International Journal of Mechanical Sciences 197 (2021) 106299

Contents lists available at ScienceDirect

International Journal of Mechanical Sciences

journal homepage: www.elsevier.com/locate/ijmecsci

The role of material and geometric nonlinearities and damping effects in designing mechanically tunable acoustic metamaterials

Shaowu Ning[a], Dongyang Chu[a], Heng Jiang[b,c,*], Fengyuan Yang[a], Zhanli Liu[a,*], Zhuo Zhuang[a]

[a] Applied Mechanics Laboratory, School of Aerospace Engineering, Tsinghua University, Beijing 100084, P.R. China
[b] Key Laboratory of Microgravity, Institute of Mechanics, Chinese Academy of Sciences, Beijing 100190, People's Republic of China
[c] University of Chinese Academy of Sciences, Beijing, 100049, People's Republic of China

ARTICLE INFO

Keywords:
Mechanically tunable acoustic metamaterials
Locally resonant
Bragg scattering
Band gaps
Material and geometrical nonlinearities
Damping effect

ABSTRACT

Elastomeric material (as rubber) can be used to design the mechanically tunable acoustic metamaterial (AM) with reversible and repeatable deformation utilizing its geometric and material nonlinearities introduced by the large deformation. Meanwhile, an elastomeric material usually possesses the inherent damping effect, which will complicate the dynamic responses of AMs. In this paper, taking the AMs comprising different resonating elements (include soft elastomeric coating and hard core) embedded into an elastomeric matrix with a square array of circular holes of varying size as examples, we try to reveal the roles of material and geometric nonlinearities and damping effects (Rayleigh damping and linear viscoelastic damping) in the process of elastic wave manipulation by calculating the band structures and the transmittances of the finite-sized AM structures with and without damping. The numerical results indicate that the geometrical nonlinearity of the AM (mainly from matrix and coating) and the nonlinearity of coating material can simultaneously manipulate the locally resonant and Bragg scattering band gaps. Still, the nonlinearity of the matrix material mainly affects the Bragg scattering band gaps. The analysis of geometrical parameters indicates that the AM with holes of large size, thin coating, and a hard core of large radius benefits enhance its bandgap's tunability. The transmittances of the finite-sized AMs without damping drastically reduce in the frequency ranges of band gaps, which agree well with the numerical predictions of band gaps. The damping effect in the elastomeric matrix and coating materials can lead to the appearance of a new band region and the changes in the position and width of the band region. However, excessive damping in the coating and matrix materials suppresses the elastic wave propagation in the AM structures so that it is difficult to identify the band regions from the transmittance spectrums. The above researches demonstrate the roles of these influencing factors above in the process of elastic wave manipulation. They can help us design new AMs to meet the unique needs of noise and vibration control.

1. Introduction

In recent years, artificially structured composite materials, such as phononic crystals and acoustic metamaterials, engineered to control and manipulate the propagation of elastic waves have received significant interest because of their broad range of applications, including wave guiding [1–3], acoustic cloaking [4,5], seismic [6,7], acoustic filter [8], wavefront modulation [9], vibration control [10–12], noise reduction [13–16], acoustic imaging and acoustic focusing [17–20]. Because of band gaps, in which the propagation of mechanical waves is forbidden, these heterogeneous systems can be exploited to suppress the noise and vibration. The band gaps mainly originate from Bragg scattering [21,22] and local resonance [23–25].

Bragg scattering band gaps in the earlier acoustic band gap material, called a phononic crystal (PC) [26,27], result from multiple scattering of waves at the interface of materials with different acoustic properties, highly depending on the periodicity and symmetry of the microstructure. The Bragg scattering band gaps typically occur at the wavelengths of the order of the structure's unit cell size. By contrast, based on localized resonance mechanism, acoustic metamaterial (AM) as a new type of human-made system exhibits unusual properties beyond natural occurring media, such as negative effective mass densities [28–30], negative effective bulk modulus [31,32], and double-negative [33–37], and so on. The AMs are especially capable of manipulating waves with wavelengths much larger than the lattice parameter of the AMs so that they can be exploited for vibration and noise control because of the low-frequency band gap characteristic of AMs. Although the development of PCs and AMs provides a new platform for manipulating the propa-

* Corresponding authors.
E-mail addresses: hengjiang@imech.ac.cn (H. Jiang), liuzhanli@tsinghua.edu.cn (Z. Liu).

https://doi.org/10.1016/j.ijmecsci.2021.106299
Received 22 September 2020; Received in revised form 19 December 2020; Accepted 19 January 2021
Available online 21 January 2021

gation of acoustic waves, many studies mainly focused on passive PCs and AMs, and their acoustic properties are fixed and difficult to change after they are fabricated, which limit their applications.

Hence, new strategies are required to design PCs and AMs with adaptive properties that can be reversibly tuned. Recently, tunable PCs and AMs based on various modulation techniques have been achieved, including AMs with piezoelectric control [15,28,38], mechanically controllable components [39–47], electric and magnetic control [29,48,49], temperature-controlled [50–52], rotation of scatterer [53,54], and so on. For the piezoelectric control strategy, active AMs were first investigated by Baz [28] and Akl and Baz [32]. They used piezoelectric materials to tune the effective density and bulk modulus of AMs. Allam et al. [38] introduced a class of active AMs consisting of clamped composite piezoelectric diaphragms suspended in air, whose effective density of the material is manipulated in real-time dynamic properties of the diaphragms through a closed-loop feedback controller. Their effective density can be programmed to any value ranging from -100 kg/m^3 to 100 kg/m^3 passing by near-zero density conditions. For a temperature-controlled strategy, Xia et al. [50] investigate the influences of the water temperature on the local resonant band gap and the negative bulk modulus of the AM with Helmholtz resonators. Results show that the relative variations of the local resonant band gap and the negative effective bulk modulus suffering from the change of the water temperature are approximately equivalent and are up to about 11%. For the electric and magnetic control strategy, Chen et al. [49] applied the principles of active AMs to membrane-type AMs by using a magnetorheological membrane material and an external gradient magnetic field to control the pre-stress inside the membrane material, and this enables the shifting of the membrane eigenfrequencies during operation by selecting appropriate external magnetic field gradients. For rotation of scatterer control strategy, Goffaux and Vigneron [53] analyzed the tunability of band gaps by altering the geometry of the PC consisting of a set of parallel solid square-section columns distributed in the air on a square lattice. Wu and Chen [54] investigated the dispersion relationship of the two-dimensional PC consisting of elliptic rods in the fluid. They found the refraction direction of the wave propagating through the PC is tuned by rotating the elliptic rods due to the geometric anisotropy of the elliptic rids. For mechanically control strategies, at present, there have been extensive studies. Fig. 1 presents several typical designs of PCs and AMs. Chen et al. [44] reported a class of mechanically tunable architected lattice metamaterials, and they possess mechanically tunable negative Poisson's ratios and vibration-mitigation capability. Utilizing the periodic porous elastomeric structures, the PCs without and with hard inclusions are designed to manipulate the elastic wave propagation in the structures through the deformation, which can refer to [41,43,45]. Wang et al. [39] reported a class of tunable and switchable AMs consisting of a metallic core connected to the elastomeric matrix through elastic beams, whose buckling is exploited as a novel and effective approach to control the elastic wave propagation.

We have known that the first AM was spherical metal cores coated with a soft rubber shell packed to a simple-cubic lattice in a host material, which could exhibit a Mie-type resonance frequency far below the wavelength-scale Bragg resonance frequency of the lattice [24]. Its dynamic property is closely related to the material and geometrical parameters of each component of this AM. Hence, if the material and geometrical parameters can be changed, its dynamic responses can be tuned correspondingly. Inspired by the above mechanically control strategies, we have designed a kind of AMs comprising resonating elements (including elastomeric coating and hard core) embedded into an elastomeric matrix with a square array of circular holes to manipulate the low-frequency locally resonant band gaps through large deformation [40]. On the one hand, the geometric and material nonlinearities of the elastomeric matrix can be induced by the large deformation. Utilizing its geometric and material nonlinearities, the tunable PCs have been designed, and the effects of geometric and material nonlinearities on their dynamic responses have been investigated [42]. On the other hand, elastomeric materials used for the matrix and coating possess the inherent damping effect, which can significantly alter the dynamic performance of PCs [41,55,56]. For AMs, we don't know what roles these effects play in tuning the dynamic responses of AMs and how they affect the dynamic responses of AMs, so that it is difficult to design the unique AMs based on the same principles to meet new needs of noise and vibration control in application.

Thus, to reveal the roles of these effects mentioned above in the process of elastic wave manipulation, taking the AMs comprising resonating elements (include elastomeric coating and hard core) embedded into an elastomeric matrix with a square array of circular holes as examples, we will investigate the effects of geometric and material nonlinearities and damping effects on the dynamic responses of AMs to reveal how to tune the responses of AMs. Through this research, we hope to provide a better understanding of the roles of design parameters in AMs and to guide us to design new AMs to meet the unique needs of noise and vibration control in application. The paper is organized as follows. The AM models investigated in this study and the corresponding governing equations, material behavior, and boundary conditions are shown in Section 2. Pattern transformation and band structures of the AMs are presented in Section 3. Section 4 highlights the roles of material and geometric nonlinearities and damping effects on band structures and transmittances of finite-sized AMs without and with damping. Additionally, the impacts of design parameters of AM on its dynamic performance is discussed in Section 5. Finally, conclusions are drawn in Section 6.

2. Numerical model description of mechanically tunable AM

A unit cell of the tunable AM, as shown in Fig. 2, is consisted of three parts: (a) soft elastomeric matrix with a square array of circular holes, (b) elastomeric coating, and (c) hard cores made of a material with reasonably high density and high rigidity [40]. The coatings and hard cores constitute the resonating elements. The large deformation of elastomeric matrix and coating under equibiaxial compression can introduce the material and geometric nonlinearities so that the dynamic responses of AMs can be tuned. In this paper, to further reveal how the deformation affects the dynamic responses of AMs, taking the AMs with different design parameters as examples, we will calculate their band structures and the transmittances of the finite-sized AMs. Here, both matrix material (a) and coating material (b) are made of hyperelasticity materials, whose responses are captured by Neo-Hookean or Gent models [42,57]. Their material parameters [40] are listed in Table 1. The geometrical parameters in Figs. 2(a), 2(b), and 2(c) can be assigned to form new and different AMs, as listed in Table 2. The areas of their coatings and hard cores are kept the same. Here, the commercial finite element code ABAQUS/Standard was used for simulating the buckling, post-buckling, and wave propagation analysis of AMs [58]. Assuming plane strain conditions, ABAQUS element type CPE6H is used to construct the finite element models. Next, the analysis process will be divided into three steps: (1) buckling analysis, (2) post-buckling analysis, and (3) wave propagation analysis [40,42].

- Buckling analysis and post-buckling analysis

It is well known that, under compression, the geometric pattern of soft periodic elastomeric cellular solids can suddenly change due to mechanical instability (microscopic instabilities or macroscopic instabilities) [43,59]. For example, for the PCs with a square array of circular holes, microscopic instabilities lead to an enlarged unit cell of 2×2 primitive unit cells and to the formation of a pattern of alternating, orthogonal and elongated holes [59]. For our designed AMs, their primitive unit cells are shown in the left subfigures of Figs. 3(a)~3(f), which are indicated by the dashed squares. Through Refined Eigen Analyses of unit cells consisting of $n \times n$ primitive unit cells [59], as shown in Fig. 4, taking Case1 and Case4.1 as examples, the critical volumetric strains that correspond to the first eigenmode converge to those of $2n \times 2n$ primitive unit cells at buckling, so that the enlarged unit cells consisting of

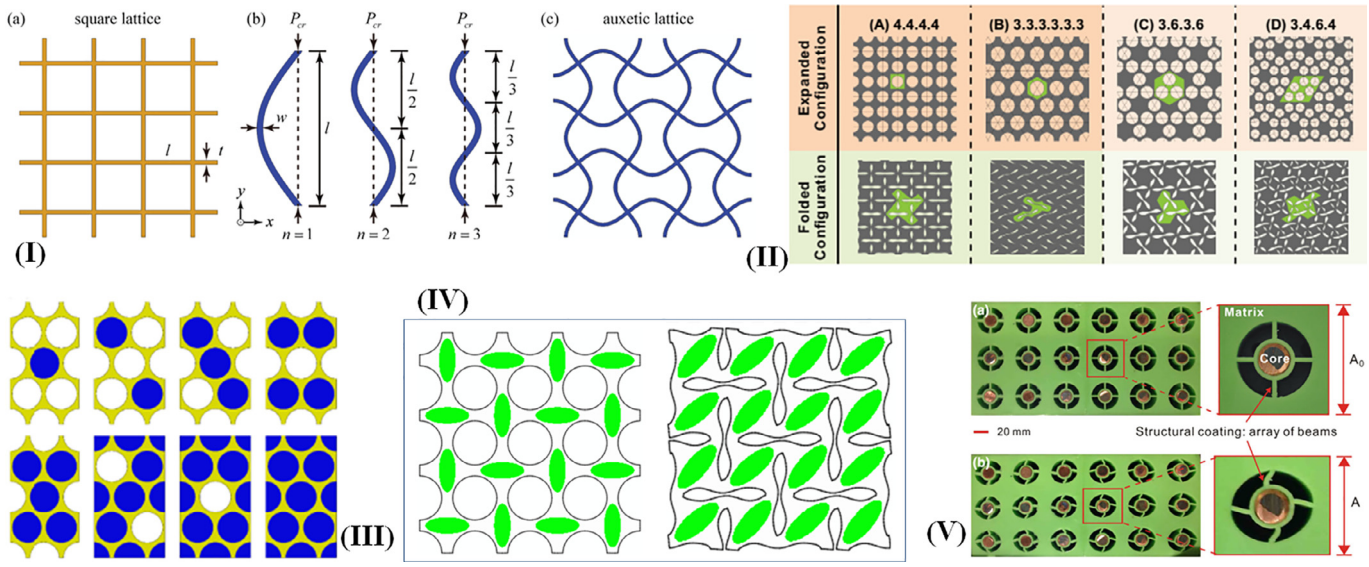

Fig. 1. Mechanically tunable phononic crystals and acoustic metamaterials. (I) Mechanically tunable lattice phononic crystals [44]. They possess mechanically tunable negative Poisson's ratios and vibration-mitigation capability; (II) Periodic porous elastomeric planar structures [43]. Their responses can be effectively tuned by the level of applied deformation; (III) Periodic porous elastomeric planar structures with hard inclusion [41]. The filled hard inclusions make the sensitivity of the post-buckling deformation to the initial geometrical imperfections significantly reduce. (IV) Periodic porous elastomeric planar structures with hard inclusion [45]. The deformation of elastomeric matrix manipulates the orientation of hard inclusion to tune the wave propagation in the structures; (V) Mechanically tunable acoustic metamaterials [39]. The buckling of elastic beams connecting the elastomeric matrix and metallic core is exploited as a novel and effective approach to control the elastic wave propagation.

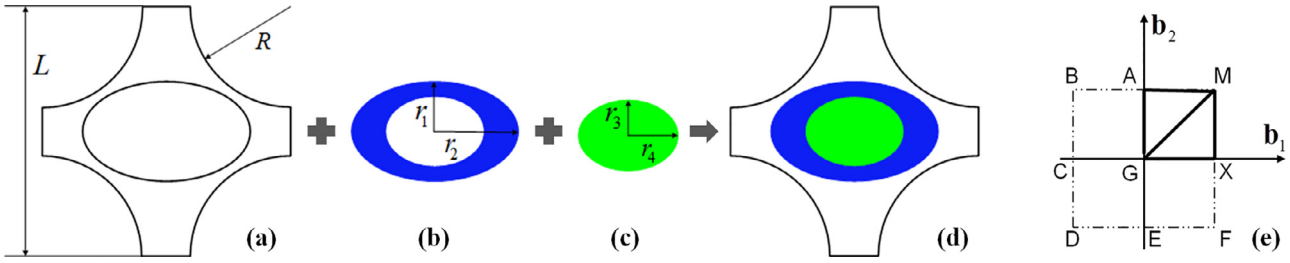

Fig. 2. Geometric parameters of AM, reciprocal lattice and the first Brillouin zone. (a) Elastomeric matrix; (b) Elastomeric coating; (c) Hard core; (d) Primitive unit cell consisting of (a), (b) and (c); (e) Reciprocal lattice and the first Brillouin zone. For (d), its IBZ is rectangle MAGXM.

Table 1
Material parameters.

Hyper-elastic: Neo-Hookean or Gent model			Elastic	
	(A) Rubber	(B) Silicone rubber		(C) Tungsten
Density (kg/m^3)	1050	1300	Density (kg/m^3)	19100
Shear modulus (MPa)	1.08	0.04	Young's modulus (MPa)	354100
Bulk modulus (MPa)	2000	2.94	Poisson's ratio	0.35

Table 2
Geometrical parameters.

	Case 1	Case 2	Case 3	Case 4	-
L (mm)	20.0	20.0	20.0	20.0	-
R (mm)	8.0	8.0	8.0	8.0	-
r_1 (mm)	5.0	5.0	4.0	4.0	$r_1 r_2 = 25$
r_2 (mm)	5.0	5.0	6.25	6.25	
r_3 (mm)	3.0	2.25	3.0	2.25	$r_3 r_4 = 9.0$
r_4 (mm)	3.0	4.0	3.0	4.0	

2×2 primitive unit cells are expected. Other AMs shown in Fig. 3 have the same characteristic. The detailed process can refer to the Supplementary Materials. In short, the deformation leads to an enlarged unit cell consisting of 2×2 primitive unit cells, as shown in the left subfigures of Figs. 3(a)~3(f). Next, the buckling analysis and post-buckling analysis will be performed on the enlarged unit cells under equibiaxial compression. In both analysis processes, continuous periodic boundary condition

$$\mathbf{u}_B - \mathbf{u}_A = \left(\bar{\mathbf{F}} - \mathbf{I}\right)\left(\mathbf{X}_B - \mathbf{X}_A\right) \tag{1}$$

is imposed on the enlarged unit cell boundaries, where A and B are two periodically located points on the boundaries of unit cells. Under equibiaxial compression, the macroscopic deformation gradient is given by $\bar{\mathbf{F}} = \lambda(\mathbf{e}_1 \otimes \mathbf{e}_1 + \mathbf{e}_2 \otimes \mathbf{e}_2)$. λ is the macroscopically applied stretch ratio and $\mathbf{e}_1$ and $\mathbf{e}_2$ are the basis vectors of two-dimensional Cartesian coordinates. Obviously, it can be noted that $\lambda = 1$, $\lambda > 1$ and $\lambda < 1$ represent the unit cell is unstretched, extended and compressed, respectively. In

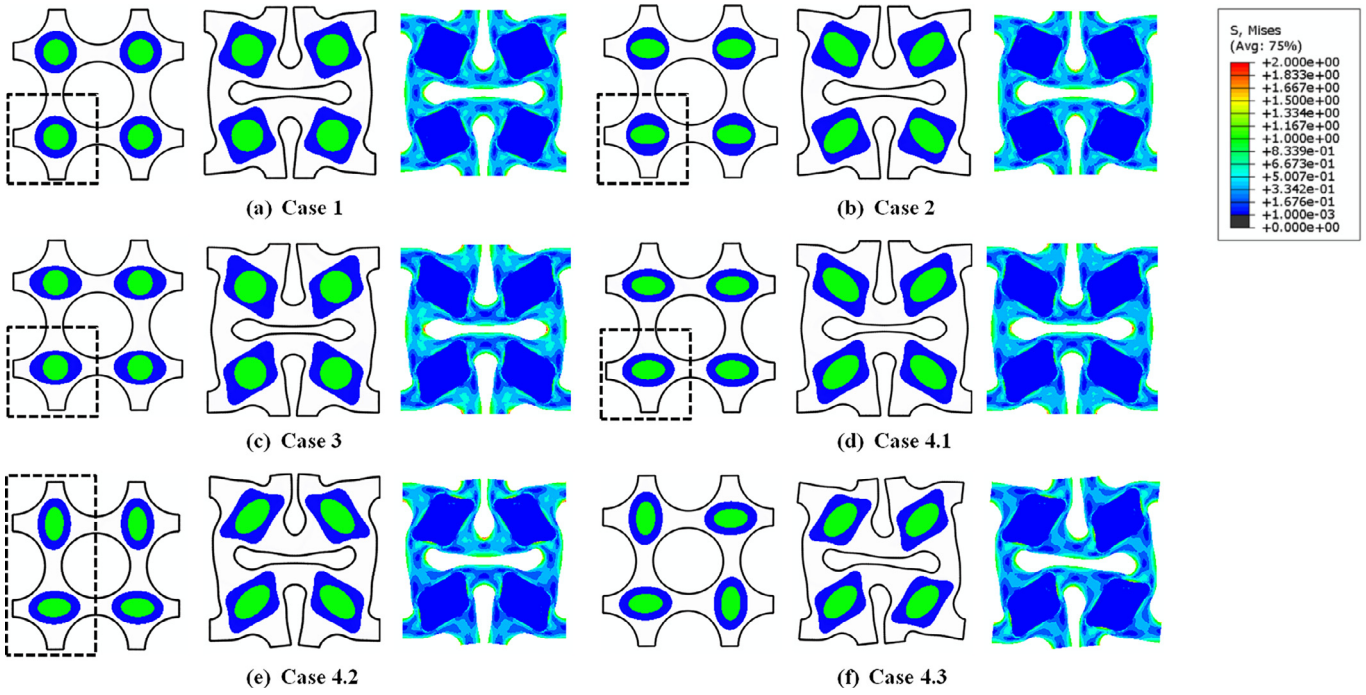

Fig. 3. The primitive and deformed unit cells of the AMs with the geometrical parameters according to Table 2 and the Mises stress distributions of the deformed configurations under equibiaxial compression ($\lambda = 0.8$). For Case 4, here are three cases with different arrangements of resonating element, as (d), (e) and (f).The dashed squares indicate the primitive unit cells.

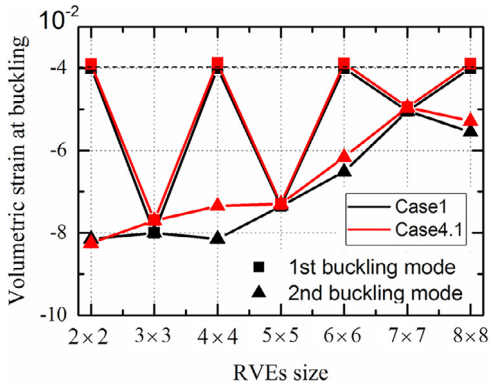

Fig. 4. Critical volumetric strains (for 1st and 2nd buckling modes) at buckling vs. unit cell sizes subjected to equibiaxial compression for Case1 and Case 4.1, respectively.

addition, note that in the process of post-buckling analysis an imperfection in the form of the lowest eigenmode scaled by the scale factor η ($\eta = 0.5$) is introduced into the initial geometry by perturbing the position of each node.

- Wave propagation analysis

In this step, frequency domain wave propagation analysis is performed on the deformed configurations to obtain the dispersion relation of AMs. To investigate the effect of the applied deformation on the propagation of small-amplitude elastic waves, incremental deformations superimposed upon a given state of finite deformation are considered. Namely, a linearized constitutive mode is used to investigate the wave propagation through the pre-deformed AM unit cells [60]. Differently, here the Bloch-type boundary condition

$$\bar{\mathbf{u}}(\mathbf{x}+\mathbf{R}) = \bar{\mathbf{u}}(\mathbf{x})\exp(\mathrm{i}\mathbf{k}\cdot\mathbf{R}) \tag{2}$$

is applied to the edges of the deformed unit cell, where $\bar{\mathbf{u}}$ and $\mathbf{x}$ denote the incremental displacement and position vector of a point, respectively, and $\mathbf{k}$ and $\mathbf{R}$ are the propagating Bloch-wave vector and the distance between each pair of nodes periodically located on the boundaries, respectively. By solving the eigenvalue problem, the dispersion relations are obtained by sweeping the wave vector $\mathbf{k} = (k_x, k_y)$ along the edges of the irreducible Brillouin zone (IBZ). It should be noted that the IBZ evolves during deformation. It is necessary to determine the IBZs according to the specific configures of unit cells (refer to Supplementary Materials). Meanwhile, the normalized frequency $\bar{f} = fl/c_t$, with f, l and $c_t = 32.07$ m/s denoting the frequency, the characteristic size of unit cell in the undeformed configuration and the elastic wave speeds for shear wave in the matrix material, is adopted in this paper.

3. Pattern transformation and Band structures of AMs

3.1. Pattern transformation

In this paper, we hope the dynamic responses of the designed AMs can be tuned by deformation. Thus, it is necessary first to investigate how the geometrical shapes of the holes, soft coating, and hard core affect the deformed configurations of the AMs. Fig. 3 shows the undeformed and deformed ($\lambda = 0.8$) configurations of unit cells and the Mises stress distributions in the deformed structures. The AMs in Figs. 3(a)~3(d) have the same radius of circular holes and different resonating elements, and the ones in Figs. 3(d)~3(f) have other arrangements of resonating elements with the same shapes. After deformation ($\lambda = 0.8$), the matrixes almost have the same deformed shapes. However, the forms of coatings significantly affect the deformed shapes of resonating elements. It can be observed from Figs. 3(a) and 3(b) that the circular coatings lead to an approximate square of resonating elements and from Figs. 3(c) ~ 3(f) that the elliptical coatings lead to an approximate parallelogram of resonating elements after deformation. Also, they can be arranged with different forms for the weak symmetric resonating elements, as shown in Figs. 3(d) ~ 3(f), and they have unique deformation patterns induced by deformation. Later we will see

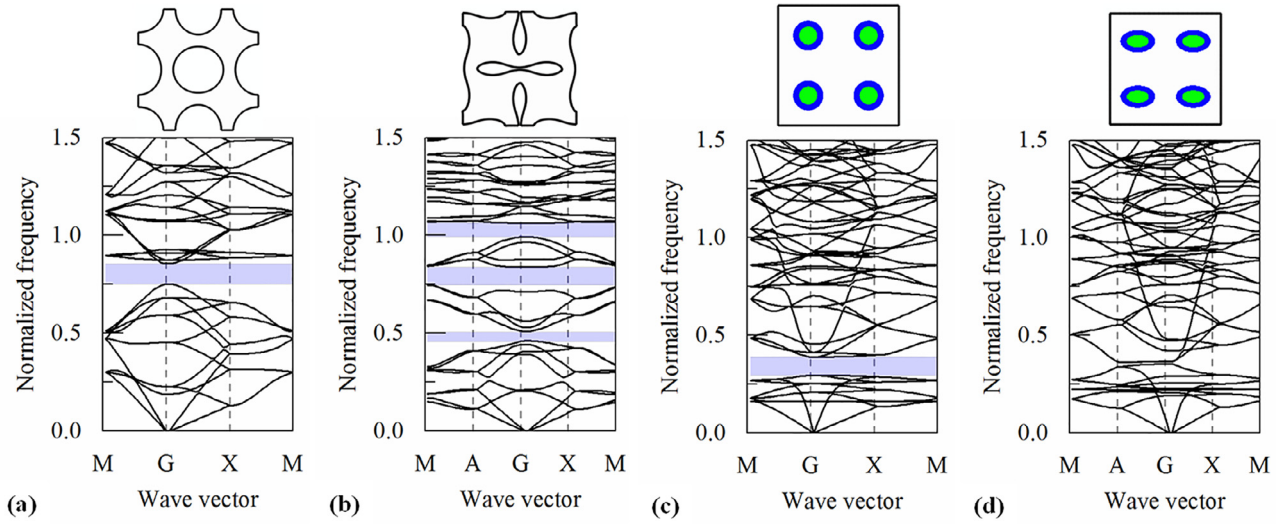

Fig. 5. Band structures. (a): The unit cell and the band structure of the pure elastomeric matrix with periodic holes with the radius 8 mm; (b): The deformed unit cell in (a) under equibiaxial compression ($\lambda = 0.8$) and the corresponding band structure; (c) and (d): The unit cells and the band structures of the elastomeric matrix only containing the resonating elements with the geometrical parameters according to Case 1 and Case 4.1, respectively. The blue bands represent the complete band gaps.

that they have different high-frequency band gap performances due to the other arrangements. Previous studies have shown that the deformations of coating and matrix materials can lead to changes in material parameters [40]. Thus I do not repeat them here, and the corresponding results are included in Supplementary Materials. Just because of the changes of geometrical shapes and material parameters during deformation, the deformation is used to tune the dynamic responses of the designed AMs. In the following, we will investigate the changes in band structures of AMs shown in Fig. 3 induced by deformation.

3.2. Band structures of the AMs

First, the designed AMs can be considered to combine the elastomeric matrix with a square array of circular holes and resonating elements (including elastomeric coating and hard core). Thus, to reveal the band gap formation mechanism of the designed AMs, we first investigate the band structures of the elastomeric matrix only with a square array of circular holes and the elastomeric matrix only with resonating elements. Figs. 5(a) and 5(b) display the band structures of the elastomeric matrix only with a square array of circular holes in the undeformed and deformed ($\lambda = 0.8$) configurations, respectively. It can be observed that after deformation, the pre-existing band gap shown in Fig. 5(a) is shifted to a new position and its width decreases, and other new band gaps are opened. These band gaps belong to the Bragg scattering band gaps. Figs. 5(c) and 5(d) show the band structures of the elastomeric matrix only with the resonating elements, whose geometrical parameters are set according to Case 1 and Case 4.1, respectively. It can be seen that there is a band gap in Fig. 5(c), which is attributed to the locally resonant of the resonating elements, but there is not a band gap in Figs. 5(d). These results indicate the geometrical shapes of the resonating elements can affect the dynamic responses of AMs. In this paper, the combinations of the combination of the elastomeric matrix with a square array of circular holes and resonating elements form the new AMs shown in Fig. 3, and later we will see that their combinations can significantly enhance the tunability of their dynamic performances.

Fig. 6 shows the band structures of AMs with the geometrical parameters according to Table 2 in the undeformed (i) and deformed (ii) configurations, respectively. Their band structures have significant differences. In comparison with Fig. 5, combining the elastomeric matrix with periodic holes and resonating elements leads to new band structures and band gaps. In the undeformed configuration, except the left figure of Fig. 6(c), there is a band gap between mode 12 and mode 13 for other cases, which corresponds to the locally resonant band gap. For these AMs, the position and width of this band gap can be tuned by deformation. These results indicate the combination of the elastomeric matrix with periodic holes and resonating elements can enhance the tunability of the dynamic response of AMs. To accurately reflect the change of the band gap before and after deformation, here we define the relative size of a band gap as [42]

$$\Delta\omega = \frac{\omega_{\text{upper}} - \omega_{\text{lower}}}{(\omega_{\text{upper}} + \omega_{\text{lower}})/2} \tag{3}$$

where ω_{upper} and ω_{lower} denote the frequencies of the upper and lower edge limits of a band gap, respectively. Table 3 lists the frequency ranges and the relative sizes of the band gaps between mode 12 and mode 13. The AMs with the parameters of Case1 and Case2, or of Case3 and Case4, have different shapes of hard cores. As listed in Table 3, the positions and widths of their band gaps between mode 12 and mode 13 have significant differences. Meanwhile, the band gaps located near the normalized frequency 1.0 are also quite different. These differences indicate the geometrical shapes of hard cores in the resonating element affect the low-frequency band gaps (locally resonant bandgap), and affect the high-frequency band gaps (Bragg scatter bandgap). In addition, for the AMs with different arrangement of resonating elements, it can be observed from Figs. 6(d)~6(f) that for the locally resonant band gaps between mode12 and mode 13, they have almost the same positions and widths in the undeformed (Fig. 6(d.i): 0.227~0.257; Fig. 6(e.i): 0.221~0.253; Fig. 6(f.i): 0.194~0.253) and deformed (Fig. 6(d.ii): 0.199~0.381, Fig. 6(e.ii): 0.189~0.376, Fig. 6(f.ii): 0.187~0.389) configurations, respectively. It is mainly because that the locally resonant band gaps are unrelated to the arrangement of resonating elements. However, their high-frequency band gaps have significant differences. The Bragg scattering band gaps are closely related to scatterers' arrangements (The resonating element plays the role of scatterer). For the Bragg scattering band gaps, both holes and resonating elements play the roles of the scatterer. The deformations of the elastomeric matrix and coating improve their coupling effects so that the tunability of Bragg scattering band gaps is significantly enhanced.

In short, the deformations of matrix and coating structures can effectively manipulate the dynamic responses of AMs. During deformation, the material and geometric nonlinearities can be induced, and they determine the manipulation of dynamic responses of AMs. Thus, it is nec-

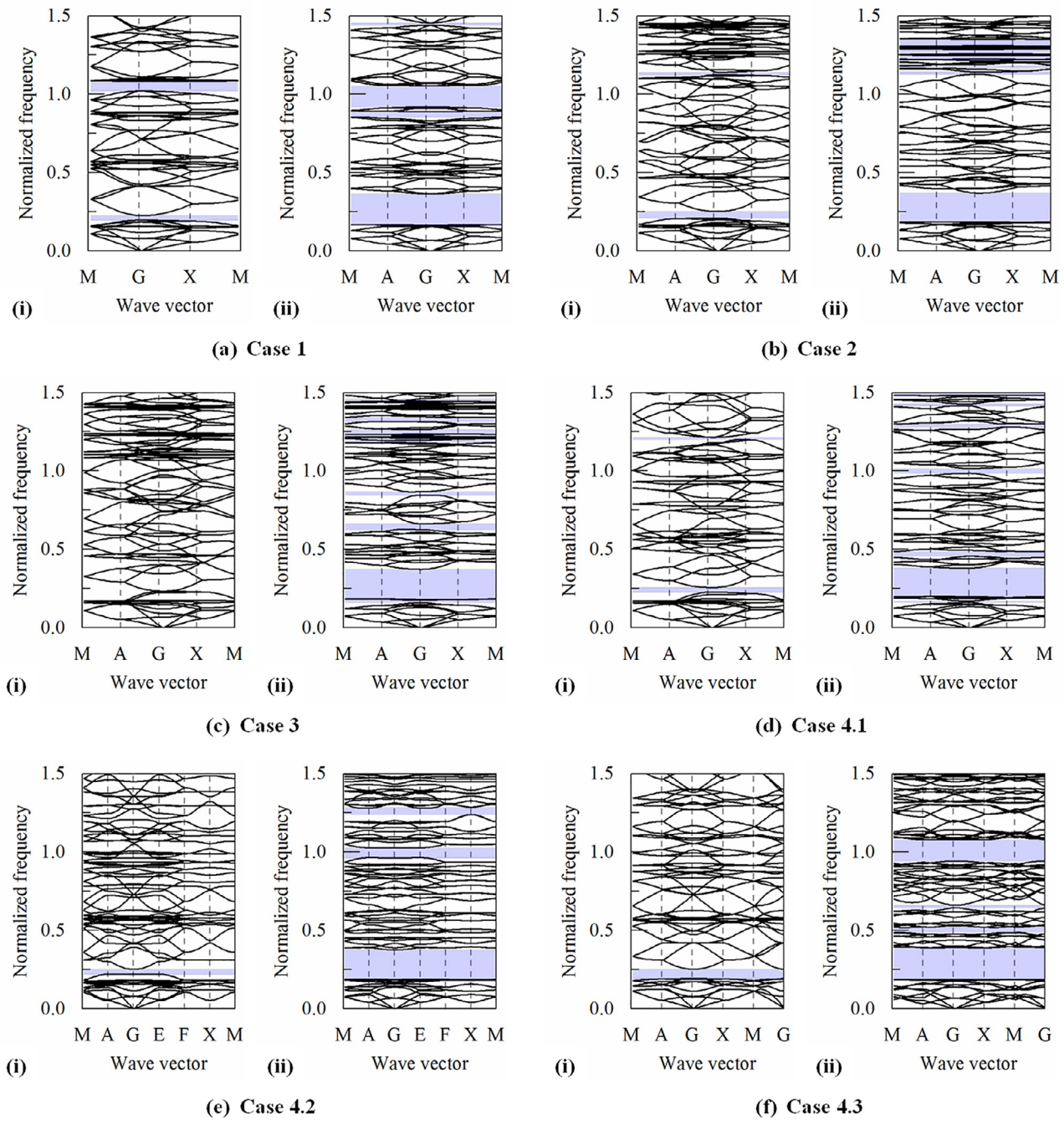

Fig. 6. Band structures of the AMs with the geometrical parameters according to Table 2 in the undeformed and deformed ($\lambda = 0.8$) configurations, respectively. For Case 4, (d), (e) and (f) are for the three cases with different arrangements of resonating element shown in Figs. 3(d), 3(e) and 3(f), respectively. (i) and (ii) are for the undeformed and deformed configurations, respectively. The blue bands represent the complete band gaps.

Table 3
The positions of the main band gaps (mode 12 ~ mode 13) and their relative sizes in Figs. 5 and 6.

Fig. 5	(a)	(b)	(c)	(d)		
Mode: 12~13	0.751~0.855	0.748~0.838	0.296~0.389	0.354~0.367		
$\Delta\omega$	0.1295	0.1135	0.2715	0.0361		
Fig. 6	(a) Case 1	(b) Case 2	(c) Case 3	(d) Case 4.1	(e) Case 4.2	(f) Case 4.3
Mode: 12~13; (i)	0.197~0.226	0.211~0.253	~	0.227~0.257	0.221~0.253	0.194~0.253
$\Delta\omega$	0.1371	0.1810	~	0.1240	0.1350	0.2640
Mode: 12~13; (ii)	0.168~0.364	0.186~0.370	0.185~0.373	0.199~0.381	0.189~0.376	0.187~0.389
$\Delta\omega$	0.7368	0.6619	0.6738	0.6276	0.6619	0.7014

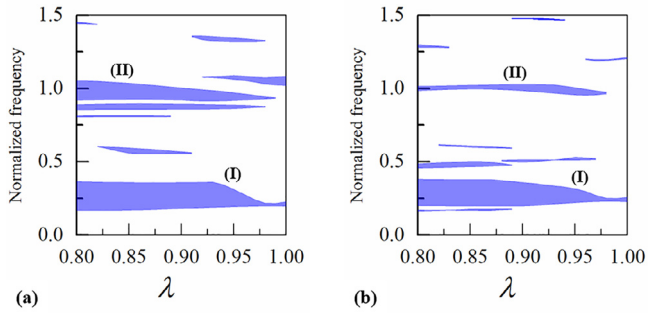

Fig. 7. Under equibiaxial compression, the evolution of band gaps as a function of stretch ratio λ for the designed AMs with the geometrical parameters according to Case1 and Case 4.1, respectively. (a) Case 1; (b) Case 4.1.

essary to investigate the roles of material and geometric nonlinearities in manipulating the dynamic responses of AMs and how to affect their dynamic responses.

4. The roles of material and geometric nonlinearities of matrix and coating materials

The above analyses have shown that the deformation can effectively manipulate the band structures of AMs. Further, taking Case1 and Case 4.1 as examples, the evolutions of band gaps as a function of the stretch ratio λ are calculated, respectively, as shown in Fig. 7. For convenience, we divide the band gaps into two groups (I) and (II). It can be seen from Figs. 7(a) and 7(b) that for the first group of band gaps (I) (between mode 12 and mode 13), it nearly remains unchanged when the stretch ratio λ is between 0.975 and 1.0. For Case1, it can be observed from Fig. 7(a) that in the compression ranges about between 0.925 and 0.975, the upper edge of the first band gap (I) significantly shifts to high-frequency. And it almost remains unchanged again when the stretch ratio is less than 0.925. The lower edge of the band gap (I) slightly moves to low-frequency in the entire compression range. Also, for the second group of band gap (II) (between mode 44 and mode 45), its position shifts to high-frequency, and its width increases with the decrease of the stretch ratio. For Case4.1, it can be observed from Fig. 7(b) that the upper edge of the first group of band gap (I) continuously shifts to high-frequency with the stretch ratio varying from 0.875 to 0.975. When the stretch ratio is less than 0.875, its upper edge almost remains unchanged. Similarly, its lower edge slightly shifts to low-frequency in the entire compression range. The evolutions of band gaps are indeed closely related to the material and geometric nonlinearities induced by deformation. However, it is unclear what roles they play in manipulating the dynamic performance of AMs during deformation. In this section, to answer this question, we first focus on the effects of material and geometric nonlinearities induced by the deformation of matrix and coating materials on the dynamic responses.

4.1. The roles of material nonlinearity of matrix and coating on the band gaps

Here, we first investigate the effect of material nonlinearity on the band gaps. In order to evaluate the effect of material nonlinearity on the dynamic response, we choose Gent constitutive model to characteristic the material properties of matrix and coating, respectively. The Gent model is characterized by the following strain energy density function [57]:

$$W(I_1, J) = -\frac{\mu}{2} J_m \log\left(1 - \frac{I_1 - 3}{J_m}\right) - \mu \log(J) + \left(\frac{\kappa}{2} - \frac{\mu}{J_m}\right)(J-1)^2 \quad (4)$$

where $I_1 = \mathrm{trace}(\mathbf{F}^T\mathbf{F})$, $J = \det(\mathbf{F})$, $\mathbf{F}$ denotes the deformation gradient and J_m denotes a material constant related to the strain at saturation. The initial shear (μ) and bulk (κ) modulus uses the same the parameters as mentioned in Table 1. Note that as $J_m \to +\infty$ the Gent model reduces to the Neo-Hookean model and the smaller values of J_m introduce stronger nonlinearities in the material behavior [42]. Taking Case 1 as an example, we investigate the dynamic responses of AMs with different Gent constitutive constants. Here, we choose four different Gent constitutive constants J_m: 0.8, 1.0, 1.5 and 5.0.

Figs. 8 and 9 show the band structures of AMs with different Gent constitutive constants J_m of coating and matrix materials, respectively. It can be seen from Fig. 8 that there is the similitude of band structures for the AMs with different Gent constitutive constants J_m, and all of the band gaps shift to low-frequency with the increase of Gent constitutive constant J_m. Here, we only focus on the band gaps (I) and (II), and they locate between mode 12 and mode 13, and between mode 44 and mode 45, respectively. Other band gaps may disappear for different Gent constitutive constants. The widths of the band gaps (I) and (II) decrease with the increase of Gent constitutive constant J_m. To quantify the changing law of the band gaps (I) and (II), Fig. 10(a) displays their relative sizes defined as Eq.(3). It can be observed from Fig. 10(a) that the relative size of the band gap (I) increases, and the band gap shifts to low-frequency with the increase of Gent constitutive constant J_m. Also, for the band gap (II), its relative size almost remains constant because it shifts to low-frequency while its width decreases. These phenomena indicate that the property of coating material can simultaneously manipulate the low- and high-frequency band gaps of the AMs. In comparison with Fig. 8, it can be seen from Fig. 9 that the band structures have small changes for different Gent constitutive constants J_m of the matrix material. Their relative sizes are shown in Fig. 10(b). It can be observed that the relative size of band gap (I) only has a few changes, but, for band gap (II) and (III), their positions shift to low-frequency and their

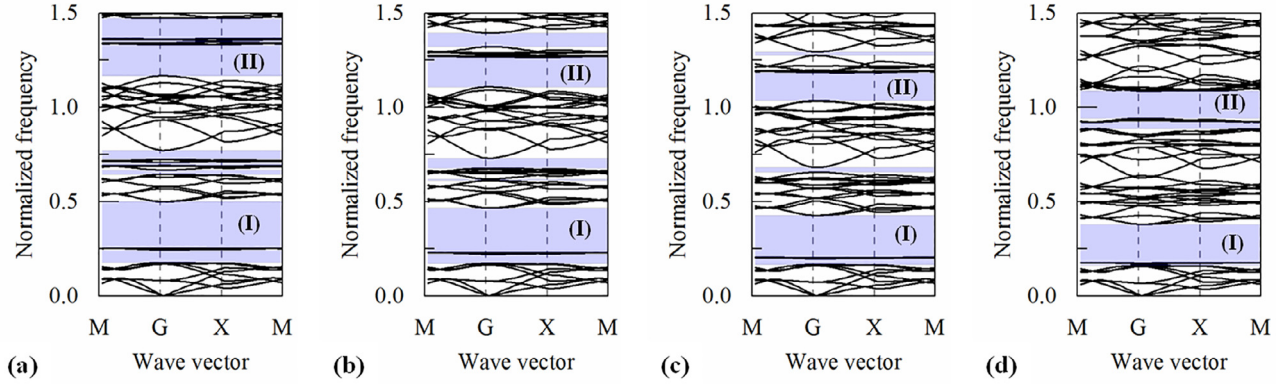

Fig. 8. The band structures of the designed AMs with the geometrical parameters according to Case1 for different Gent constitutive constants J_m of coating material. (a) $J_m = 0.8$; (b) $J_m = 1.0$; (c) $J_m = 1.5$; (d) $J_m = 5.0$.

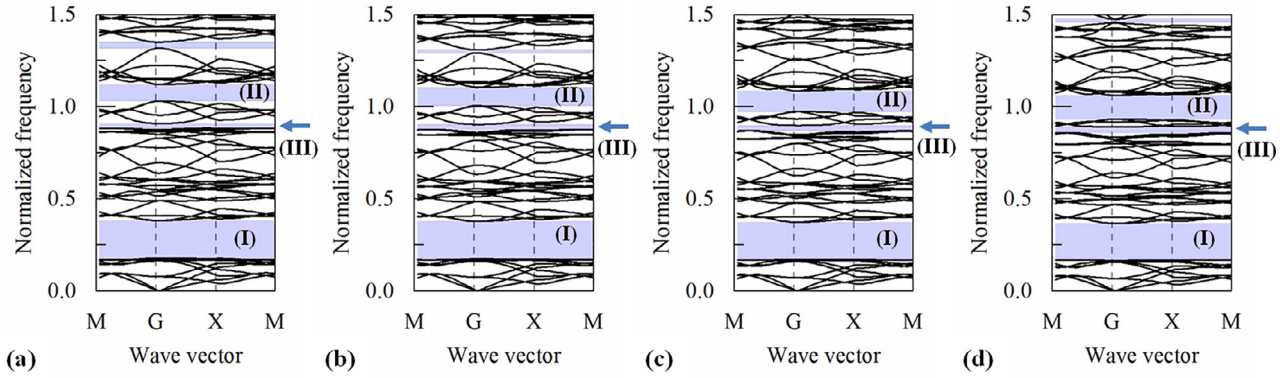

Fig. 9. The band structures of the designed AMs with the geometrical parameters according to Case 1 for different Gent constitutive constants J_m of matrix material. (a) $J_m = 0.8$; (b) $J_m = 1.0$; (c) $J_m = 1.5$; (d) $J_m = 5.0$.

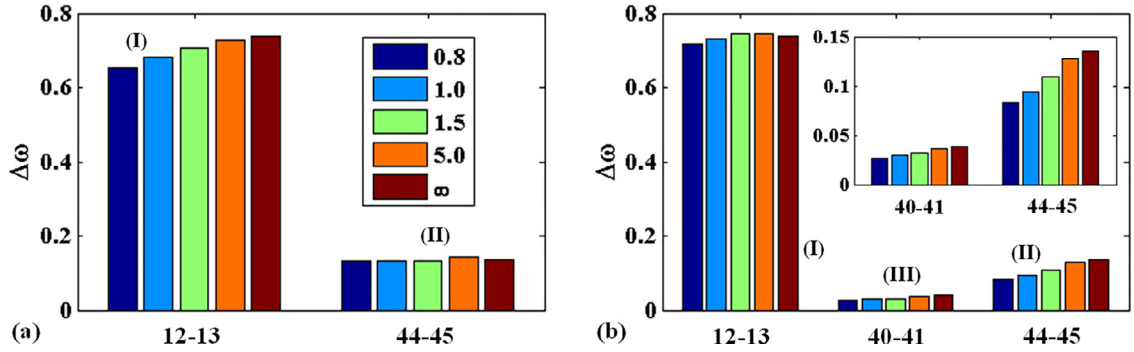

Fig. 10. The relative size of the main band gaps in Figs. 8 and 9 of the AMs with the geometrical parameters according to Case 1 for different Gent constitutive constants. The band gaps (I), (II) and (III) are between mode 12 and mode 13, mode 44 and mode 45, and mode 40 to mode 41, respectively. (a): coating material; (b): matrix material.

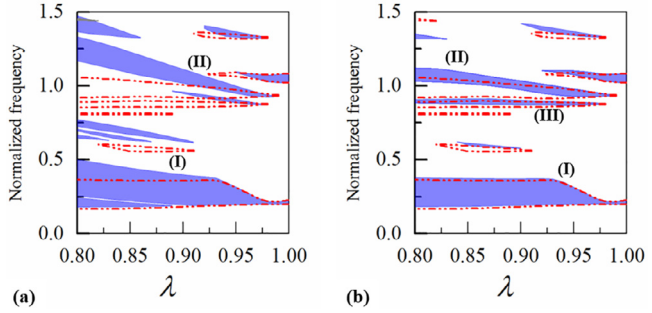

Fig. 11. The evolution of band gaps as a function of stretch ratio λ for the AMs with the geometrical parameters according to Case 1. The Gent constitutive constant J_m of both coating and matrix materials are 0.8 and other parameters remain unchanged. (a) Coating material. (b) Matrix material. The red lines represent the band gaps shown in Fig. 7(a).

relative sizes increase with the increase of Gent constitutive constant J_m. These phenomena indicate that the property of matrix material can significantly affect their high-frequency band gaps (Bragg scattering band gap (II) and (III)) but slightly affect the low-frequency band gap (locally resonating band gap (I)) of the AMs. In short, the tunability of locally resonating band gaps (I) is mainly related to the coating material.

Further, taking Case 1 as an example, Fig. 11 shows the evolution of band gaps as a function of stretch ratio λ for the designed AMs. The Gent constitutive constants J_m of coating and matrix materials are 0.8, representing the elastomeric material is strong nonlinearity, and other parameters remain unchanged. Firstly, it can be observed from Figs. 7 and 11 that the first group of band gaps (I) (between mode 12 and mode 13) nearly remains unchanged when the stretch ratio λ is between 0 and -0.025. In fact, for them, in this stretch range, the coating still works in an elastic state during compression, and their geometrical shapes only have small changes so that their dynamic performances remain unchanged. However, in other stretch ranges, there are significant differences between Fig. 11(a) and Fig. 7(a). These differences are attributed to the strong material nonlinearity of coating material. Differently, it can be seen from Fig. 11(b) that the strong nonlinearity of matrix material almost doesn't affect the band gap (I), but other band gaps can be significantly changed. These results demonstrate the strong nonlinear coating material can simultaneously enhance the tunability of the low- and high-frequency dynamic responses. The strong nonlinear matrix material only affects the tunability of the high-frequency dynamic response. In addition to playing the role of the local resonance, the resonant element also plays the role of the scatterer. Thus the nonlinearity of coating material can simultaneously alter the locally resonating and Bragg scattering band gaps. By contrast, because the nonlinearity of matrix material only affects the wave propagation in the matrix, it significantly affects Bragg scattering band gaps. Still, it does not affect the locally resonant band gaps.

4.2. The roles of geometric nonlinearity of matrix and coating on the band gaps

Next, to evaluate the effect of geometric nonlinearity on the dynamic responses of the AMs, we investigate the dynamic responses in a stress-free structure with the deformed geometry determined by the post-buckling analysis. After deformation, we set all the stress components to zero before performing the dynamic response analysis. Namely, the inhomogeneous stress distribution is not taken into consideration when computing the dynamic response. Figs. 12(a) and 12(b) show the

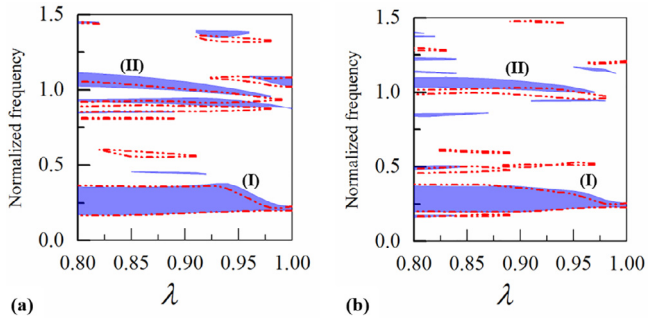

Fig. 12. The evolution of band gaps as a function of stretch ratio λ for the designed AMs in the stress-free structures with the deformed geometries, whose initial material parameters and geometrical parameters set according to Case 1 and Case 4.1, respectively. (a) Case 1; (b) Case 4.1. The red lines represent the band gaps shown in Fig. 7.

evolution of band gaps as a function of stretch ratio λ for the designed AM as Case 1 and Case 4.1, respectively. Their material parameters are set with the initial material parameters. The red lines in Fig. 12 represent the band gaps shown in Fig. 7. These results indicate the large deformation (geometrical nonlinearity) can significantly manipulate their dynamic responses. Especially, the small differences between locally resonant band gaps (I) shown in Fig. 12 and Fig. 7 indicate they mainly come from their geometrical deformation when the materials of AMs are weakly nonlinear. Other band gaps shown in Fig. 12 can be significantly tuned by deformation. Their differences shown in Fig. 12 and Fig. 7 are due to the absence of material nonlinearity. They indicate again that the tunability of the Bragg scattering band gap results from the comprehensive action of the geometric and material nonlinearities of the AMs during deformation.

4.3. Transmittances of mechanically tunable finite-sized AMs and the role of material damping effect

Usually, to enhance the tunable ability, the matrix and coating materials of AMs are composed of soft elastomeric materials. Besides the above material and geometric nonlinearities, the soft materials usually present significant viscous and damping effects, which have a remarkable impact on elastic wave propagating in the AM structures. Here, by calculating the transmittances of finite-sized AMs without and with damping, we study the damping effects in the matrix and coating materials on their dynamic responses.

4.3.1. Mechanically tunable finite-sized AM structures and their transmittances without damping

To validate the tunability of dynamic responses of the designed AMs, two samples of the AMs comprising 8 × 8 unit cells shown in Fig. 3(a) and 4 × 4 unit cells shown in Fig. 3(f) are chosen to calculate their dynamic responses in the undeformed and deformed ($\lambda = 0.8$) configurations. Here the monopole excitation in-plane is applied to excite the dynamic responses of the AM structures, and it is approximated by a radial pressure excitation, as shown in Fig. 13. Letter A denotes the input measurement location, and letter B and C represent the output measurement locations, whose accurate positions are exhibited in Figs. 14(a) and 15(a). The initial configurations of the AM structures are shown in Figs. 14(a) and 15(a), and their deformed configurations are demonstrated in Figs. 14(b) and 15(b), respectively. Figs. 14(c) and 15(c) show the transmittance spectrums of the finite-sized AMs in the undeformed and deformed configurations, respectively. The transmittance is defined as $20\log_{10}(|u_{out}|/|u_{in}|)$, where $|u_{out}|$ and $|u_{in}|$ are the amplitudes of displacements in the output and input measuring positions, respectively. The upper and lower figures of Figs. 14(c) and 15(c) display the transmittance curves from A to B and from A to C, respectively. In these figures, the gray and red bands represent the band gaps in the undeformed and deformed ($\lambda = 0.8$) configurations. Luckily, it can be observed from Figs. 14(c) and 15(c) that the transmittances significantly reduce in the frequency ranges of band gaps, and they agree well with the numerical predictions of band gaps above. However, it should also be observed from Fig. 14(c) that there are significant inconsistencies between the low-frequency locally resonant band gap and the band region in the transmittance spectrum in the undeformed configuration. The discrepancies are mainly due to the influence of the boundaries of finite-sized AM structures. Also, besides the complete band gaps, we can observe that the transmittances significantly attenuate in some frequency ranges, for example, in the frequency range between 0.5 and 0.75 and near 1.25, which is attributed to the existence of directional band gaps. These results indicate the tunability of the AM structures' dynamic responses through deformation, especially for the low-frequency locally resonant band regions.

4.3.2. The roles of damping effects in mechanically tunable finite-sized AM structures

For the finite-sized AMs with damping, to reveal the roles of damping effects in the mechanically tunable finite-sized AM structures, we respectively define the material with Rayleigh damping and viscoelastic damping material to investigate the influences of damping effects on the finite-sized AM structures' dynamic responses.

4.3.2.1. Rayleigh damping. For convenience, we only specify Rayleigh damping factor β for stiffness proportional damping in ABAQUS/Standard. Thus, an additional damping stress σ_d proportions to the total strain rate, $\sigma_d = \beta D^{el}\dot{\varepsilon}$, where $\dot{\varepsilon}$ is the strain rate. For hyperelastic material D^{el} is defined as the elastic stiffness in the strain-free state [58]. Here, we take the finite-sized AM structures as shown in Figs. 16(a) and 16(b) as examples and six groups of damping factors β, such as 0 (Undamped), 1e-5, 1e-4, 0.001, 0.01 and 0.03, are chosen to calculate its transmittances from A to C in the undeformed and deformed configurations. These results are shown in Fig. 16. The gray and red bands in Fig. 16 denote the band gaps shown in Fig. 6(f) in the undeformed and deformed configurations. It can be observed that, in comparison with the undamped case, the Rayleigh damping makes the transmittances of the AM structures attenuate obviously in the pass-bands. Especially, the attenuation in the high-frequency range (greater than the locally resonant band gap) is more significant.

Fig. 16(a) shows the effects of the matrix materials with different damping factors on the transmittances of the finite-sized AM structures. The top and bottom halves of Fig. 16(a) are for the undeformed and deformed configurations, respectively. It can be seen from Fig. 16(a) that for these cases, the band regions disappear gradually with an increase of the damping factors, so that it is difficult to identify the band regions from the transmittance spectrums. For example, for damping factor 1e-5, we still clearly recall the three band regions (the gray band in the upper figure and the two red bands in the lower figure). Yet, for the cases with damping equal or greater than 0.001, these band regions disappear. Also, it is seen that the transmittances increase with the increase of damping factors equal to or greater than 0.001. It is attributed to the fact that, on the one hand, an excessive amount of damping is equivalent to increasing the stiffness of the structures. On the other hand, it can impede the relative motion within the structures to consume energy. Thus, excessive damping enhances the wave transmittances in the AM structures.

Fig. 16(b) shows the effects of the coating materials with different damping factors on the transmittances of the finite-sized AM structures. The top and bottom halves of Fig. 16(b) are for the undeformed and deformed configurations, respectively. Besides the same characteristics as those shown in Fig. 16(a), it can be observed from the top half of Fig. 16(b) that there is a valley in the normalized frequency range 0.6~1.0 when the damping factors are 0.01 and 0.03, respectively. Meanwhile,

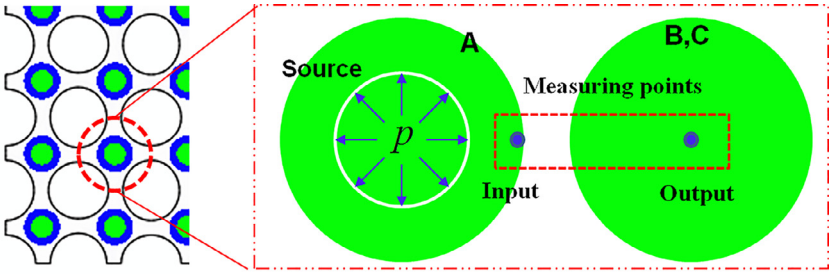

Fig. 13. The radial pressure excitation method, which is used to approximate the monopole excitation, and Input (A) and Output (B,C) denote the measuring positions of the input and output signals.

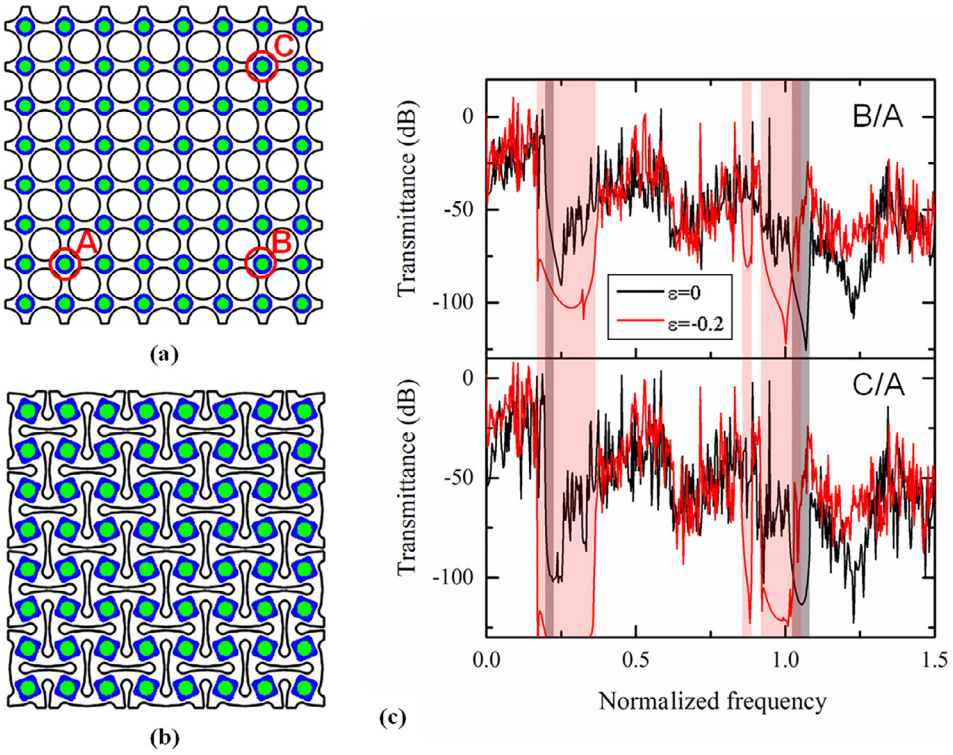

Fig. 14. Finite-sized AM structure with 8 × 8 unit cells with geometrical parameters according to Case 1 in the undeformed (a) and deformed (b, $\lambda = 0.8$) configurations and their transmittance curves (c). Letter A denotes the input measurement location. Letter B and C denote the output measurement locations. The gray and red bands denote the band gaps shown in Fig. 6(a) in the undeformed and deformed ($\lambda = 0.8$) configurations, respectively.

in the bottom half of Fig. 16(b), we can observe that the normalized frequency range of the valley widens to 0.6~1.4. As explained above, the excessive amount of damping in coating material increases the coating's stiffness and impedes the occurrence of local resonance. A resonating element (including coatings and hard cores) translates to a scatterer so that the Bragg scattering phenomenon appears. And this valley corresponds to the Bragg scattering band gap. This exciting interesting phenomenon can help us to design other tunable acoustic metamaterials through material damping effects. Also, these results indicate that for the Rayleigh damping model, the damping factor needs to be optimized rather than bigger is better to achieve the most effective suppressive of elastic wave propagation.

4.3.2.2. Linear viscoelastic damping. In contrast, a linear viscoelastic damping model based on frequency domain Prony series is adopted to investigate the influences of damping effect on the dynamic responses of the finite-sized AM structures. The expression for the frequency-dependent shear modulus can be written as follows [58]:

$$G_s(\omega) = G_0 G_s^*, G_s^*(\omega) = \left[1 - \sum_{i=1}^{N} \bar{g}_i^P\right] + \sum_{i=1}^{N} \frac{\bar{g}_i^P \tau_i^2 \omega^2}{1 + \tau_i^2 \omega^2} \tag{5}$$

$$G_l(\omega) = G_0 G_l^*, G_l^*(\omega) = \sum_{i=1}^{N} \frac{\bar{g}_i^P \tau_i \omega}{1 + \tau_i^2 \omega^2} \tag{6}$$

$$\tan\delta = \frac{G_l}{G_s} = \frac{G_l^*}{G_s^*} \tag{7}$$

where $\bar{g}_i^P$, τ_i and $i = 1, 2, \cdots, N$, are material constants. G_0 is the instantaneous shear modulus, $G_s(\omega)$ is the storage modulus, $G_l(\omega)$ is the loss modulus, ω is the angular frequency, and N is the number of terms in the Prony series. We don't consider the viscoelastic damping associated with the bulk modulus. Here, to facilitate the parametric study, the first-order Prony series is chosen in the frequency domain, $N = 1$. The influences of viscoelastic damping on the dynamic characteristics of AMs are investigated by adopting different material parameters τ_1 and $\bar{g}_1^P$. First, the material parameter τ_1 is chosen as 1e-4s, 1e-3s, 0.01s, and 0.1s, respectively, while the parameter $\bar{g}_1^P$ is fixed at 0.5. Fig. 17(a) shows the evolutions of the storage and loss shear moduli verse frequency at the given parameter τ_1. It can be seen that the smaller the parameter τ_1 is, the greater the loss shear modulus is so that the greater the loss factor tan δ is. Further, the parameter $\bar{g}_1^P$ is chosen as 0.25, 0.5, and 0.75, respectively, while τ_1 is fixed at 1e-4s. Fig. 17(b) shows the evolutions of the storage and loss shear moduli verse frequency at the given parameter $\bar{g}_1^P$. It can be observed from Fig. 17(b) that the greater the parameter $\bar{g}_1^P$ is, the smaller the loss shear modulus is, so that the greater the loss factor tan δ is. Next, we respectively discuss the effects of the material parameters τ_1 and $\bar{g}_1^P$ in the viscoelastic damping model on the wave transmittances in the finite-sized AM structures.

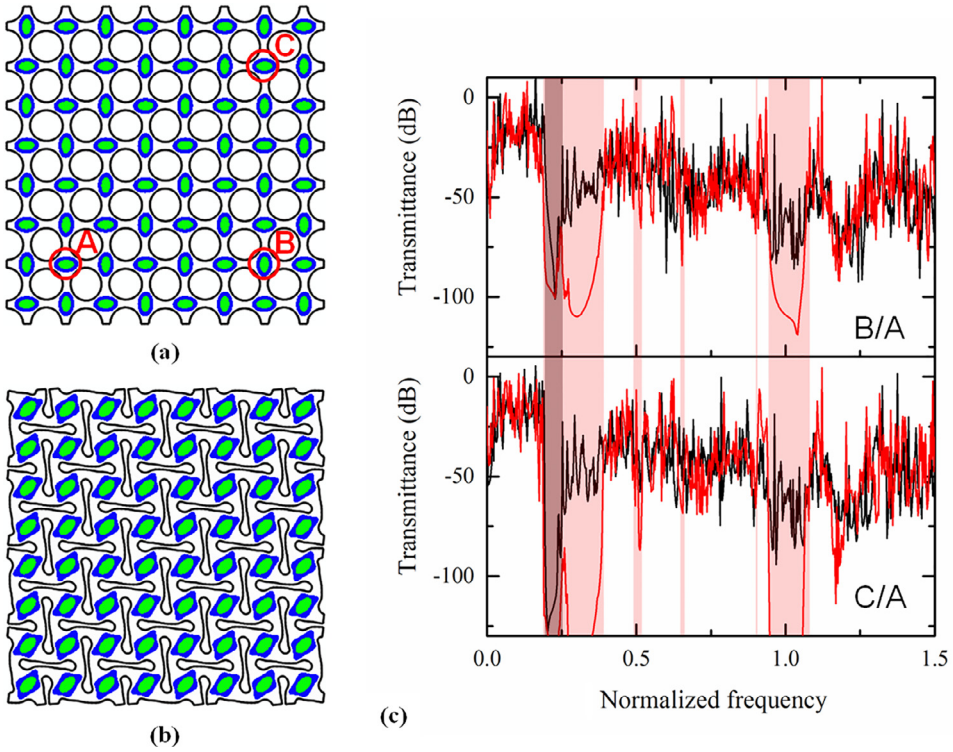

Fig. 15. Finite-sized AM structure with 4 × 4 unit cells with geometrical parameters according to Case 4.3 in the undeformed (a) and deformed (b, $\lambda = 0.8$) configurations and their transmittance curves (c). The gray and red bands denote the band gaps shown in Fig. 6(f) in the undeformed and deformed ($\lambda = 0.8$) configurations, respectively.

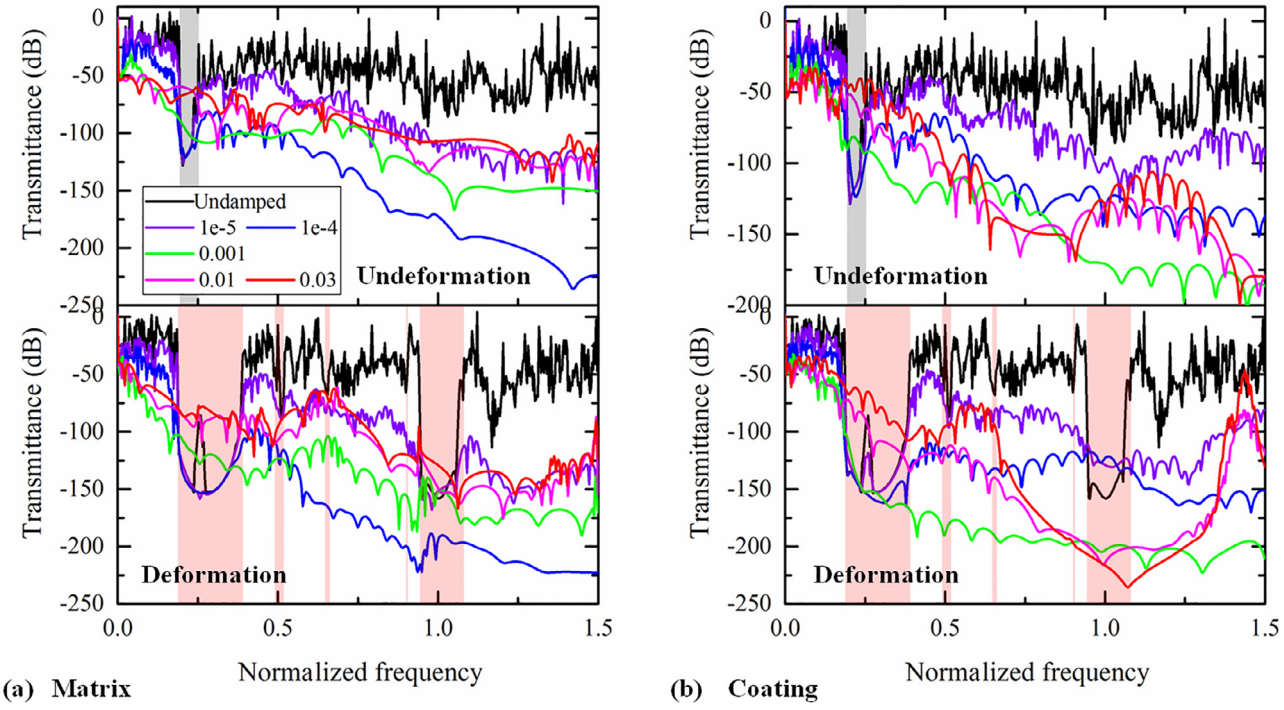

Fig. 16. The effects of the damping effects of matrix and coating materials on the transmittances from A to C in the finite-sized AM structures with 4 × 4 unit cells according to Case 4.3. (a) is for matrix material and (b) for coating material. The gray and red bands denote the band gaps shown in Fig. 6(f) in the undeformed and deformed configurations, respectively. The damping factors β are 1e-5, 1e-4, 0.001, 0.01 and 0.03, respectively.

Figs. 18 and 19 show the effects of the material parameter $\bar{g}_1^P$ on the transmittances of the finite-sized AM structures. Here the parameter τ_1 is fixed at 1e-4s and 0.1s, respectively. And Fig. 20 shows the effects of the material parameter τ_1 on the transmittances of finite-sized AM structures. Here the parameter $\bar{g}_1^P$ is fixed at 0.5. In these figures, the gray and red bands denote the band gaps (as shown in Fig. 6(f)) of AMs without damping in the undeformed and deformed configurations, respectively. As described above, a small parameter τ_1 or a large parameter $\bar{g}_1^P$ means large viscous damping in the viscoelastic material. Similar to Fig. 16, it can be seen from Figs. 18 and 20 that excessive viscous damping can effectively suppress the dynamic responses of the

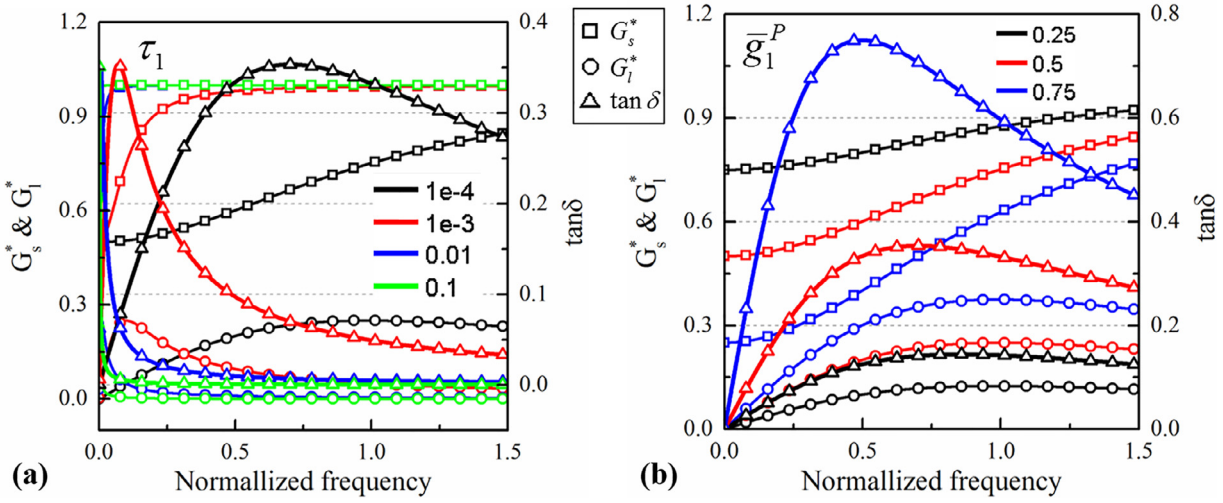

Fig. 17. The evolutions of the storage and loss shear moduli verse frequency at the given parameters τ_1 and $\bar{g}_1^P$, respectively. (a) τ_1: 1e-4, 1e-3, 0.01 and 0.1; (b) $\bar{g}_1^P$: 0.25, 0.5, 0.75.

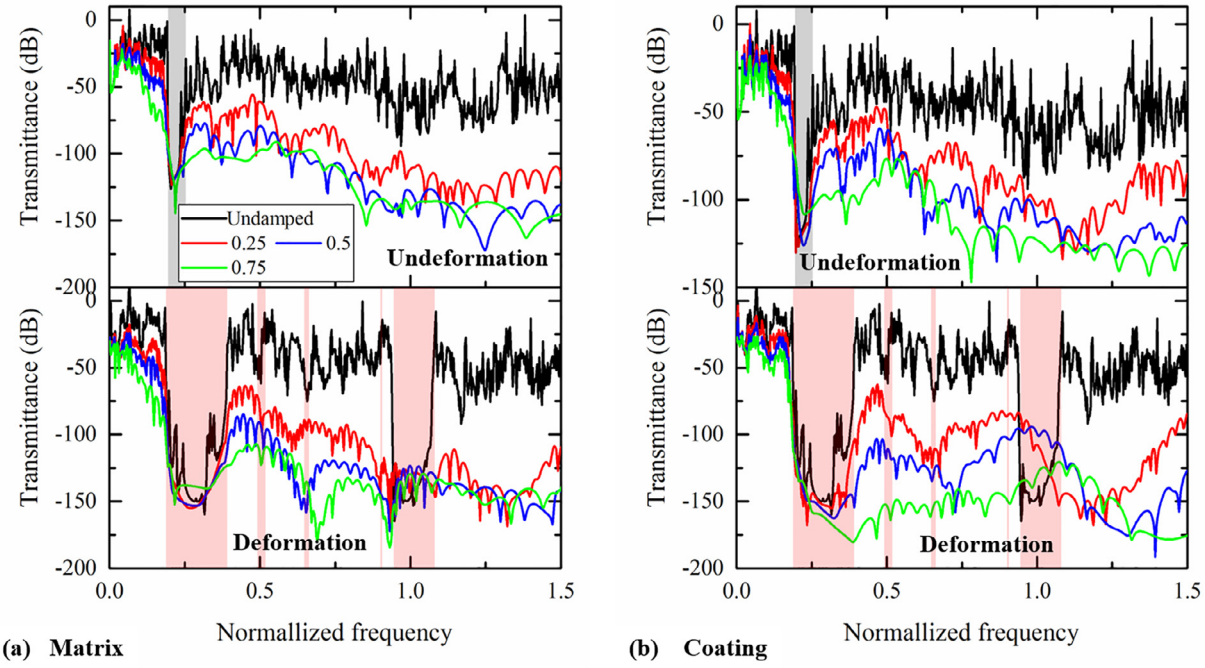

Fig. 18. The effects of the viscoelastic damping parameter $\bar{g}_1^P$ of matrix and coating materials on the transmittances from A to C in the finite-sized AM structures with 4 × 4 unit cells according to Case 4.3. (a) is for matrix material and (b) for coating material. The gray and red bands denote the band gaps shown in Fig. 6(f) in the undeformed and deformed configurations, respectively. The viscoelastic damping parameter $\bar{g}_1^P$ is selected as 0.25, 0.5 and 0.75, respectively, while the parameter τ_1 is fixed at 1e-4s.

finite-sized AM structures in the high-frequency range so that the band regions can't be identified from the transmittance spectrums.

In Fig. 18, the parameter τ_1 is fixed at 1e-4s, and this means that sizeable viscous damping is contained in the matrix and coating materials. Thus, the high-frequency responses are suppressed so that it is difficult to identify the high-frequency Bragg scattering band regions from the transmittance spectrums. However, the low-frequency locally resonant band regions still can be identified from Fig. 18. In Fig. 19, the parameter τ_1 is fixed at 0.1s. In comparison with Fig. 18, there is small viscous damping in the matrix and coating materials. Interestingly, in contrast with those without damping and with Rayleigh damping, some new phenomena can be observed from the transmittance spectrums. For the case that the matrix material adopts the viscoelastic damping model, the high-frequency Bragg scattering band regions are opened after deformation, and the low-frequency locally resonant and high-frequency Bragg scattering band regions shift to high-frequency with the increase of parameter $\bar{g}_1^P$, as shown in Fig. 19(a). It can be noted that the transmittances inside these band regions increase with the rise of parameter $\bar{g}_1^P$ before and after deformation, and excessive damping makes the high-frequency Bragg scattering band region disappear, such as $\bar{g}_1^P = 0.75$. For the case that the coating material adopts the viscoelastic damping model, besides the low-frequency locally resonant band region, a new high-frequency Bragg scattering band region is opened in the undeformed configuration when the parameter $\bar{g}_1^P$ is greater than a special value. For example, for the cases of $\bar{g}_1^P = 0.5$ and $\bar{g}_1^P = 0.75$, the band regions at about 1.13~1.28 and 1.24~1.48 are opened, respectively. This

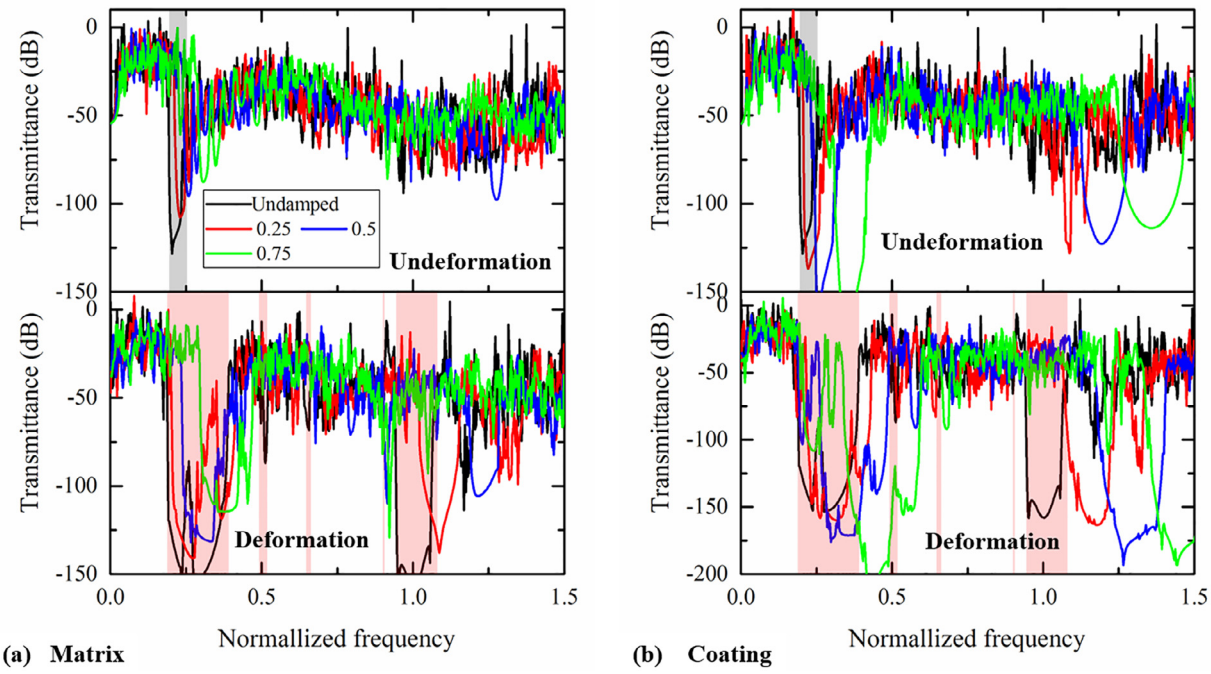

Fig. 19. The effects of the viscoelastic damping parameter $\bar{g}_1^P$ of matrix and coating materials on the transmittances from A to C in the finite-sized AM structures with 4 × 4 unit cells according to Case 4.3. The material parameter τ_1 is fixed at 0.1s, and other parameters are the same as those in Fig. 18.

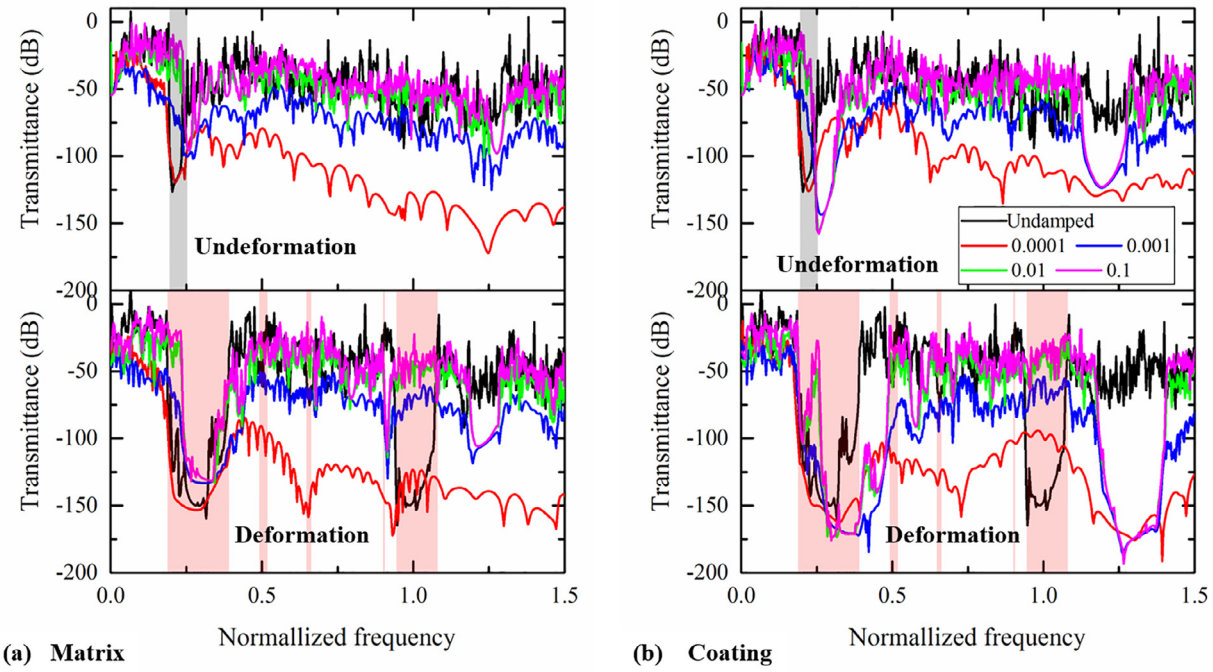

Fig. 20. The effects of the viscoelastic damping parameter τ_1 of matrix and coating materials on the transmittances from A to C in the finite-sized AM structures with 4 × 4 unit cells according to Case 4.3. (a) is for matrix material and (b) for coating material. The gray and red bands denote the band gaps shown in Fig. 6(f) in the undeformed and deformed configurations, respectively. The viscoelastic damping parameter τ_1 is selected as 1e-4s, 0.001s, 0.01s and 0.1s, respectively, while the parameter $\bar{g}_1^P$ is fixed at 0.5.

phenomenon is not observed in the cases without damping and with Rayleigh damping. By contrast, this new band region's appearance in the undeformed configuration is attributed to the frequency-dependent of viscoelastic damping material. Similarly, after deformation, the low-frequency locally resonant and high-frequency Bragg scattering band regions shift to high-frequency with the increase of parameter $\bar{g}_1^P$. Also, it can be noted from Fig. 19 that the width of the high-frequency Bragg scattering band region also increases with the rise of the parameter $\bar{g}_1^P$. Differently, the transmittances inside these band regions decrease with the increase of parameter $\bar{g}_1^P$ before and after deformation.

In Fig. 20, the material parameter $\bar{g}_1^P$ is fixed at 0.5, and the effects of the material parameter τ_1 on the dynamic responses of the finite-sized AM structures are investigated. It can be seen from Fig. 20 that the low-frequency locally resonant band region shifts to the high-frequency

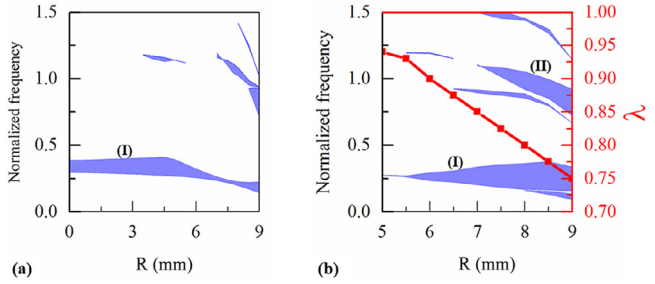

Fig. 21. Effect of radius of circular hole on band gaps of the AM with geometrical parameters according to Case 1. (a) and (b) are for the undeformed and deformed configurations, respectively. The red line in (b) shows the adopted stretch ratios for different radiuses of circular holes.

range with the increase of viscoelastic damping parameters τ_1 before and after deformation. The smaller the parameter τ_1 is, the greater the damping in the material is. Thus, when the parameter τ_1 is 1e-4s, it is difficult to identify the high-frequency Bragg scattering band region from the transmittance spectrum. Also, in comparison with the undamped case, the existence of viscoelastic damping makes the high-frequency Bragg scattering band region shift to the high-frequency range. Especially, when the coating material adopts the viscoelastic damping material model with parameters $\tau_1 = 0.001$, 0.01, and 0.1, it can be observed from the top half of Fig. 20(b) that the new high-frequency Bragg scattering band region at about 1.125~1.284 can be opened in the undeformed configuration. These band regions have the same positions and widths. It can be seen by combining Fig. 19 and Fig. 20 that the material parameter $\bar{g}_1^P$ determines the position and width of the high-frequency Bragg band region. In comparison with those without damping and with Rayleigh damping (Fig. 16), the appearance of this band region is closely related to the frequency-dependent of viscoelastic damping material and material parameters $\bar{g}_1^P$ and τ_1.

In short, because of the frequency-dependent of viscoelastic damping material, the valleys in the transmittance spectrums, which correspond to the band gaps, exhibit the dependency of viscoelastic damping material parameters. The band regions are different for different viscoelastic damping material parameters $\bar{g}_1^P$ and τ_1. We can design other tunable AMs utilizing the frequency-dependent of viscoelastic material damping effects based on these phenomena,

5. Discussion of design parameters of AM

The above analyses focus on the effects of material and geometric nonlinearities and damping effects of matrix and coating materials on the dynamic responses of AMs. To enhance the tunability of the dynamic performance of AM, besides the above factors, the rational design of AM can further promote its dynamic performance and tunability. The results shown in Fig. 6 indicate that the geometrical shapes of components of AMs can affect their dynamic performance. In this section, we also discuss the effect of the geometrical parameter of AM on its dynamic responses. Here, taking Case 1 as the example, Figs. 21, 22, and 23 display the effects of the radius of circular holes, the coating's thickness, and the radius of hard core on its dynamic response.

Fig. 21 shows the effects of the radius of circular holes on the band gaps of the AMs in the undeformed and deformed configurations, respectively. Except for the radius of the circular holes, other parameters remain constant according to Case 1. It can be observed from Fig. 21(a) that there is a band gap (I), which is between mode 12 and mode 13, and its position and width vary with the radius of the circular holes. The holes of considerable size in the elastomeric matrix lead to enhancing the coupling effect between resonating elements and holes in the elastomeric matrix. The locally resonant band gap varies with the radius of the circular holes. Meanwhile, other band gaps (except the band gap (I)) appear after the radius of the circular hole is greater than a specified

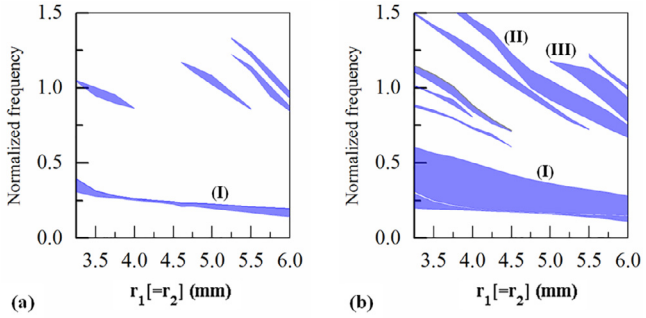

Fig. 22. Effects of thickness of coating on band gaps of the AM with geometrical parameters according to Case 1. (a) and (b) are for the undeformed and deformed ($\lambda = 0.8$) configurations, respectively.

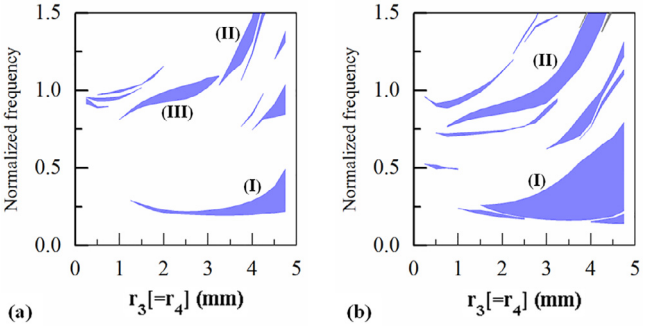

Fig. 23. Effects of radius of hard core on band gaps of the AM with geometrical parameters according to Case 1. (a) and (b) are for the undeformed and deformed ($\lambda = 0.8$) configurations, respectively.

value (7mm). The holes of large size can enhance the wave scattering effect in the matrix to result in the Bragg scattering band gap.

Because the size of the circular hole in the elastomeric matrix limits the deformation of the elastomeric matrix, we adopt suitable stretch ratios to induce the deformations of matrixes with different circular holes. The red line in Fig. 21(b) represents the adopted stretch ratios for the matrixes with different radius of the circular holes. It can be seen that the width of the band gap (I) between mode 12 and mode 13 significantly increases, and its position shifts to high-frequency with the increase of the radius of circular hole. Meanwhile, when the radius of the circular hole is greater than 7 mm, the new band gap (II) between mode 44 and mode 45 appears, which corresponds to the wave Bragg scattering band gap. With the increase of the hole's radius, its width significantly increases, and its position shifts to low-frequency. In short, the AMs with holes of large size have better tuning performance. On the one hand, the large size hole enhances the wave Bragg scattering effect in the matrix. On the other hand, it allows the large deformation of the elastomeric matrix to manipulate the elastic wave propagation.

Fig. 22 shows the effects of the thickness of the coating on the band gaps of the AMs in the undeformed and deformed configurations, respectively. Except for the thickness of coating, other parameters are the same as Case 1. It can be observed from Fig. 22(a) that all of the band gaps are shifted to low-frequencies with the increase of thickness of the coating. By contrast, there are more band gaps in the deformed configuration, as shown in Fig. 22(b). Especially, for the band gap (I) between mode 12 and mode 13, it can be significantly tuned through deformation, and the thinner the thickness of the coating, the wider the width of the band gap after deformation. Meanwhile, the Bragg scattering band gaps between mode 44 and mode 45 (II), mode 52 and mode 53 (III) appear when the thickness is more significant than a specified value. Their positions shift to low-frequency while their widths are widened with the increase of the coating's thickness in the deformed configuration. The

resonating element (including coating and hard cores) can play the role of the scatterer. The deformation of the elastomeric matrix and coating further enhances the coupling effects of holes and coating so that the Bragg scattering band gaps are significantly tuned during deformation. Also, the thick coating means that the coating has a weak equivalent stiffness, and thus the locally resonating band gap (I) is shifted to low-frequency with the increase of thickness of the coating. Fig. 23 shows the effects of the radius of hard core on the band gaps of the AMs in the undeformed and deformed configurations. Increasing the radius of the hard core is similar to decreasing the thickness of the coating, and thus we can get the same conclusions from Fig. 23 as those from Fig. 22.

In short, the results shown in Figs. 21, 22, and 23 demonstrate that the large-sized holes, thin coatings, and large-sized hard cores in AMs benefit them to acquire the optimal manipulation performance of dynamic response. According to the engineering requirement, the AM's design needs to be chosen carefully to meet the design target.

6. Conclusions

To reveal the roles of the geometric, material, and damping parameters in mechanically tunable AMs in manipulating the elastic wave propagation, taking the AMs comprising resonating element (include soft elastomeric coating and hard core) embedded into an elastomeric matrix with a square array of circular holes as examples, their band structures and the transmittances of finite-sized AM structures are calculated to investigate the influences of these parameters above on the tunability of their dynamic responses. The conclusions are gotten as follows:

1. The deformation (geometric nonlinearity) of elastomeric matrix and coating induced by equibiaxial compression can simultaneously manipulate their low-frequency (locally resonating) and high- frequency (Bragg scattering) band gaps. The AM with holes of large size, thin coating, and a hard core of large radius benefits enhance the band gap's tunability and has a wider band gap. The resonating element's arrangement mainly affects the Bragg scattering band gaps because the locally resonant band gap is unrelated to its arrangement.
2. The stronger nonlinearity of coating material can simultaneously manipulate their low- (locally resonating) and high- frequency (Bragg scattering) band gaps during deformation. Still, the nonlinearity of matrix material mainly tunes their high-frequency (Bragg scattering) band gaps.

The transmittances of the finite-sized AM structures without damping agree well with the numerical predictions of band gaps, which validate the tunability of the dynamic responses of the AMs. However, the damping effect in the elastomeric matrix and coating materials can lead to the appearance of a new band region and the changes in the position and width of the band region. This phenomenon can guide us in designing new AMs to manipulate the wave propagation. However, excessive damping in the matrix and coating materials makes it hard for us to identify the band regions from the transmittances of the finite-sized AM structures.

In summary, the paper's results can guide us to design various tunable AMs to meet the new needs of elastic wave propagation manipulation. Significantly, the low-frequency locally resonant band gap can be tuned by deformation to be used for low-frequency noise and vibration control. The optimal damping needs to be optimized rather than bigger to achieve the most effective suppressive of elastic wave propagation through the damping effect.

Declaration of Competing Interest

The authors declare that they have no known competing financial interests or personal relationships that could have appeared to influence the work reported in this paper.

CRediT authorship contribution statement

Shaowu Ning: Conceptualization, Methodology, Writing - original draft. **Dongyang Chu:** Software, Data curation. **Heng Jiang:** Conceptualization. **Fengyuan Yang:** Software, Data curation. **Zhanli Liu:** Conceptualization, Writing - review & editing. **Zhuo Zhuang:** Conceptualization, Writing - review & editing.

Acknowledgments

This work is supported by the Science Challenge Project, No. TZ2018002 (TZ2018001), National Natural Science Foundation of China, under Grant No. 11972205, 11722218 and 11921002, the National Key Research Development Program of China (No. 2017YFB0702003), Opening Project of Applied Mechanics and Structure Safety Key Laboratory of Sichuan Province.

Supplementary materials

Supplementary material associated with this article can be found, in the online version, at doi:10.1016/j.ijmecsci.2021.106299.

References

[1] Wang Y-F, Wang T-T, Liang J-W, Wang Y-S, Laude V. Channeled spectrum in the transmission of phononic crystal waveguides. J Sound Vib 2018;437:410–21. doi:10.1016/j.jsv.2018.09.030.
[2] Oudich M, Assouar MB, Hou Z. Propagation of acoustic waves and waveguiding in a two-dimensional locally resonant phononic crystal plate. Appl Phys Lett 2010;97:193503. doi:10.1063/1.3513218.
[3] Casadei F, Delpero T, Bergamini A, Ermanni P, Ruzzene M. Piezoelectric resonator arrays for tunable acoustic waveguides and metamaterials. J Appl Phys 2012;112:064902. doi:10.1063/1.4752468.
[4] Zigoneanu L, Popa BI, Cummer SA. Three-dimensional broadband omnidirectional acoustic ground cloak. Nat Mater 2014;13:352–5. doi:10.1038/nmat3901.
[5] Zhang S, Xia C, Fang N. Broadband Acoustic Cloak for Ultrasound Waves. Phys Rev Lett 2011;106:024301. doi:10.1103/PhysRevLett.106.024301.
[6] Brûlé S, Javelaud EH, Enoch S, Guenneau S. Experiments on Seismic Metamaterials: Molding Surface Waves. Phys Rev Lett 2014;112:133901. doi:10.1103/PhysRevLett.112.133901.
[7] Achaoui Y, Ungureanu B, Enoch S, Brûlé S, Guenneau S. Seismic waves damping with arrays of inertial resonators. Extrem Mech Lett 2016;8:30–7. doi:10.1016/j.eml.2016.02.004.
[8] Chen Z-G, Zhao J, Mei J, Wu Y. Acoustic frequency filter based on anisotropic topological phononic crystals. Sci Rep 2017;7:15005. doi:10.1038/s41598-017-15409-2.
[9] Zhao S-D, Chen A-L, Wang Y-S, Zhang C. Continuously Tunable Acoustic Metasurface for Transmitted Wavefront Modulation. Phys Rev Appl 2018;10:054066. doi:10.1103/PhysRevApplied.10.054066.
[10] Claeys CC, Vergote K, Sas P, Desmet W. On the potential of tuned resonators to obtain low-frequency vibrational stop bands in periodic panels. J Sound Vib 2013;332:1418–36. doi:10.1016/j.jsv.2012.09.047.
[11] Casadei F, Beck BS, Cunefare KA, Ruzzene M. Vibration control of plates through hybrid configurations of periodic piezoelectric shunts. J Intell Mater Syst Struct 2012;23:1169–77. doi:10.1177/1045389X12443014.
[12] Wu X, Sun L, Zuo S, Liu P, Huang H. Vibration reduction of car body based on 2D dual-base locally resonant phononic crystal. Appl Acoust 2019;151:1–9. doi:10.1016/j.apacoust.2019.02.020.
[13] Xiao Y, Wen J, Wen X. Sound transmission loss of metamaterial-based thin plates with multiple subwavelength arrays of attached resonators. J Sound Vib 2012;331:5408–23. doi:10.1016/j.jsv.2012.07.016.
[14] Casadei F, Dozio L, Ruzzene M, Cunefare KA. Periodic shunted arrays for the control of noise radiation in an enclosure. J Sound Vib 2010;329:3632–46. doi:10.1016/j.jsv.2010.04.003.
[15] Zhang H, Wen J, Xiao Y, Wang G, Wen X. Sound transmission loss of metamaterial thin plates with periodic subwavelength arrays of shunted piezoelectric patches. J Sound Vib 2015;343:104–20. doi:10.1016/j.jsv.2015.01.019.
[16] Brooke DC, Umnova O, Leclaire P, Dupont T. Acoustic metamaterial for low frequency sound absorption in linear and nonlinear regimes. J Sound Vib 2020;485:115585. doi:10.1016/j.jsv.2020.115585.
[17] Qiu C, Zhang X, Liu Z. Far-field imaging of acoustic waves by a two-dimensional sonic crystal. Phys Rev B 2005;71:054302. doi:10.1103/PhysRevB.71.054302.
[18] Kaina N, Lemoult F, Fink M, Lerosey G. Negative refractive index and acoustic superlens from multiple scattering in single negative metamaterials. Nature 2015;525:77–81. doi:10.1038/nature14678.
[19] Chen J, Xiao J, Lisevych D, Shakouri A, Fan Z. Deep-subwavelength control of acoustic waves in an ultra-compact metasurface lens. Nat Commun 2018;9:4920. doi:10.1038/s41467-018-07315-6.
[20] Dong H-W, Zhao S-D, Wang Y-S, Zhang C. Broadband single-phase hyperbolic elastic metamaterials for super-resolution imaging. Sci Rep 2018;8:2247. doi:10.1038/s41598-018-20579-8.

[21] Hussein MI, Hulbert GM, Scott RA. Dispersive elastodynamics of 1D banded materials and structures: Analysis. J Sound Vib 2006;289:779–806. doi:10.1016/j.jsv.2005.02.030.
[22] Kushwaha MS, Halevi P, Dobrzynski L, Djafari-Rouhani B. Acoustic band structure of periodic elastic composites. Phys Rev Lett 1993;71:2022–5. doi:10.1103/PhysRevLett.71.2022.
[23] Zhou X, Liu X, Hu G. Elastic metamaterials with local resonances: an overview. Theor Appl Mech Lett 2012;2:041001. doi:10.1063/2.1204101.
[24] Liu Z. Locally Resonant Sonic Materials. Science 2000;289:1734–6 80-. doi:10.1126/science.289.5485.1734.
[25] Ma G, Sheng P. Acoustic metamaterials: From local resonances to broad horizons. Sci Adv 2016;2 e1501595. doi:10.1126/sciadv.1501595.
[26] Hussein MI, Leamy MJ, Ruzzene M. Dynamics of Phononic Materials and Structures: Historical Origins, Recent Progress, and Future Outlook. Appl Mech Rev 2014;66:040802 38 pages. doi:10.1115/1.4026911.
[27] Lu M-H, Feng L, Chen Y-F. Phononic crystals and acoustic metamaterials. Mater Today 2009;12:34–42. doi:10.1016/S1369-7021(09)70315-3.
[28] Baz A. The structure of an active acoustic metamaterial with tunable effective density. New J Phys 2009;11:123010. doi:10.1088/1367-2630/11/12/123010.
[29] Bou Matar O, Robillard JF, Vasseur JO, Hladky-Hennion A-C, Deymier PA, Pernod P, et al. Band gap tunability of magneto-elastic phononic crystal. J Appl Phys 2012;111:054901. doi:10.1063/1.3687928.
[30] Yao S, Zhou X, Hu G. Experimental study on negative effective mass in a 1D mass–spring system. New J Phys 2008;10:043020. doi:10.1088/1367-2630/10/4/043020.
[31] Fang N, Xi D, Xu J, Ambati M, Srituravanich W, Sun C, et al. Ultrasonic metamaterials with negative modulus. Nat Mater 2006;5:452–6. doi:10.1038/nmat1644.
[32] Akl W, Baz A. Multi-cell active acoustic metamaterial with programmable bulk modulus. J Intell Mater Syst Struct 2010;21:541–56. doi:10.1177/1045389X09359434.
[33] Zhu R, Liu XN, Hu GK, Sun CT, Huang GL. Negative refraction of elastic waves at the deep-subwavelength scale in a single-phase metamaterial. Nat Commun 2014;5:5510. doi:10.1038/ncomms6510.
[34] Yang M, Ma G, Yang Z, Sheng P. Coupled Membranes with Doubly Negative Mass Density and Bulk Modulus. Phys Rev Lett 2013;110:134301. doi:10.1103/PhysRevLett.110.134301.
[35] Lee SH, Park CM, Seo YM, Wang ZG, Kim CK. Composite Acoustic Medium with Simultaneously Negative Density and Modulus. Phys Rev Lett 2010;104:054301. doi:10.1103/PhysRevLett.104.054301.
[36] Ding Y, Liu Z, Qiu C, Shi J. Metamaterial with Simultaneously Negative Bulk Modulus and Mass Density. Phys Rev Lett 2007;99:093904. doi:10.1103/PhysRevLett.99.093904.
[37] Li Z, Wang C, Wang X. Modelling of elastic metamaterials with negative mass and modulus based on translational resonance. Int J Solids Struct 2019;162:271–84. doi:10.1016/j.ijsolstr.2018.12.015.
[38] Allam A, Elsabbagh A, Akl W. Experimental demonstration of one-dimensional active plate-type acoustic metamaterial with adaptive programmable density. J Appl Phys 2017;121:125106. doi:10.1063/1.4979020.
[39] Wang P, Casadei F, Shan S, Weaver JC, Bertoldi K. Harnessing Buckling to Design Tunable Locally Resonant Acoustic Metamaterials. Phys Rev Lett 2014;113:014301. doi:10.1103/PhysRevLett.113.014301.
[40] Ning S, Yang F, Luo C, Liu Z, Zhuang Z. Low-frequency tunable locally resonant band gaps in acoustic metamaterials through large deformation. Extrem Mech Lett 2020;35:100623. doi:10.1016/j.eml.2019.100623.
[41] Li J, Wang Y, Chen W, Wang Y-S, Bao R. Harnessing inclusions to tune post-buckling deformation and bandgaps of soft porous periodic structures. J Sound Vib 2019;459:114848. doi:10.1016/j.jsv.2019.114848.
[42] Wang P, Shim J, Bertoldi K. Effects of geometric and material nonlinearities on tunable band gaps and low-frequency directionality of phononic crystals. Phys Rev B 2013;88:014304. doi:10.1103/PhysRevB.88.014304.
[43] Shim J, Wang P, Bertoldi K. Harnessing instability-induced pattern transformation to design tunable phononic crystals. Int J Solids Struct 2015;58:52–61. doi:10.1016/j.ijsolstr.2014.12.018.
[44] Chen Y, Li T, Scarpa F, Wang L. Lattice Metamaterials with Mechanically Tunable Poisson's Ratio for Vibration Control. Phys Rev Appl 2017;7:024012. doi:10.1103/PhysRevApplied.7.024012.
[45] Ning S, Luo C, Yang F, Liu Z, Zhuang Z. Mechanically Tunable Solid/Solid Phononic Crystals Through the Rearrangement of Hard Scatterers Controlled by the Deformation of Periodic Elastomeric Matrixes. J Appl Mech 2020;87. doi:10.1115/1.4047365.
[46] Wang YT, Liu XN, Zhu R, Hu GK. Wave propagation in tunable lightweight tensegrity metastructure. Sci Rep 2018;8:11482. doi:10.1038/s41598-018-29816-6.
[47] Wang Y, Zhao W, Rimoli JJ, Zhu R, Hu G. Prestress-controlled asymmetric wave propagation and reciprocity-breaking in tensegrity metastructure. Extrem Mech Lett 2020;37:100724. doi:10.1016/j.eml.2020.100724.
[48] Wu B, Zhou W, Bao R, Chen W. Tuning Elastic Waves in Soft Phononic Crystal Cylinders Via Large Deformation and Electromechanical Coupling. J Appl Mech 2018;85:031004 16 pages. doi:10.1115/1.4038770.
[49] Chen X, Xu X, Ai S, Chen H, Pei Y, Zhou X. Active acoustic metamaterials with tunable effective mass density by gradient magnetic fields. Appl Phys Lett 2014;105:071913. doi:10.1063/1.4893921.
[50] Xia B, Chen N, Xie L, Qin Y, Yu D. Temperature-controlled tunable acoustic metamaterial with active band gap and negative bulk modulus. Appl Acoust 2016;112:1–9. doi:10.1016/j.apacoust.2016.05.005.
[51] Nimmagadda C, Matlack KH. Thermally tunable band gaps in architected metamaterial structures. J Sound Vib 2019;439:29–42. doi:10.1016/j.jsv.2018.09.053.
[52] Billon K, Ouisse M, Sadoulet-Reboul E, Collet M, Butaud P, Chevallier G, et al. Design and experimental validation of a temperature-driven adaptive phononic crystal slab. Smart Mater Struct 2019;28:035007. doi:10.1088/1361-665X/aaf670.
[53] Goffaux C, Vigneron JP. Theoretical study of a tunable phononic band gap system. Phys Rev B 2001;64:075118. doi:10.1103/PhysRevB.64.075118.
[54] Wu L-Y, Chen L-W. The dispersion characteristics of sonic crystals consisting of elliptic cylinders. J Phys D Appl Phys 2007;40:7579–83. doi:10.1088/0022-3727/40/23/051.
[55] Sharma GS, Skvortsov A, MacGillivray I, Kessissoglou N. Acoustic performance of periodic steel cylinders embedded in a viscoelastic medium. J Sound Vib 2019;443:652–65. doi:10.1016/j.jsv.2018.12.013.
[56] Lewińska MA, Kouznetsova VG, van Dommelen JAW, Krushynska AO, Geers MGD. The attenuation performance of locally resonant acoustic metamaterials based on generalised viscoelastic modelling. Int J Solids Struct 2017. doi:10.1016/j.ijsolstr.2017.08.003.
[57] Gent AN. A new constitutive relation for rubber. Rubber Chem Technol 1996;69:59–61. doi:10.5254/1.3538357.
[58] Abaqus Simulia DS, Fallis A, Techniques D. Abaqus Analysis User's Guide (6.14). Abaqus 2013;612. doi:10.1017/CBO9781107415324.004.
[59] Bertoldi K, Boyce MC, Deschanel S, Prange SM, Mullin T. Mechanics of deformation-triggered pattern transformations and superelastic behavior in periodic elastomeric structures. J Mech Phys Solids 2008;56:2642–68. doi:10.1016/j.jmps.2008.03.006.
[60] Bertoldi K, Boyce MC. Wave propagation and instabilities in monolithic and periodically structured elastomeric materials undergoing large deformations. Phys Rev B 2008;78:184107. doi:10.1103/PhysRevB.78.184107.